Studying the warm hot intergalactic medium in emission: a reprise

G. Parimbelli [1,2,3,4,5,6]* E. Branchini,[1,2,3] M. Viel,[4,5,6,7] F. Villaescusa-Navarro[8,9] and J. ZuHone[10]

[1]*Dipartimento di Fisica, Università degli studi di Genova, via Dodecaneso 33, I-16146 Genova, Italy*
[2]*Dipartimento di Matematica e Fisica. Università Roma Tre, via della Vasca Navale 84, I-00146 Rome, Italy*
[3]*INFN – Istituto Nazionale di Fisica Nucleare, via della Vasca Navale 84, I-00146 Rome, Italy*
[4]*Scuola Internazionale Superiore di Studi Avanzati, via Bonomea 265, I-34136 Trieste, Italy*
[5]*INAF-OATs, Osservatorio Astronomico di Trieste, via Tiepolo 11, I-34131 Trieste, Italy*
[6]*IFPU – Institute for Fundamental Physics of the Universe, via Beirut 2, I-34151 Trieste, Italy*
[7]*INFN – Istituto Nazionale di Fisica Nucleare, via Valerio 2, I-34127 Trieste, Italy*
[8]*Center for Computational Astrophysics, Flatiron Institute, 162 5th Avenue, New York, NY 10010, USA*
[9]*Department of Astrophysical Sciences, Princeton University, Peyton Hall, Princeton, NJ 08544, USA*
[10]*Center for Astrophysics, Harvard & Smithsonian, 60 Garden Street, Cambridge, MA 02138, USA*

ABSTRACT

The warm-hot intergalactic medium (WHIM) contains a significant portion of the 'missing baryons'. Its detection in emission remains a challenge. Integral field spectrometers like X-IFU on board of the Athena satellite will secure WHIM detection in absorption and emission and, for the first time, allow us to investigate its physical properties. In our research, we use the CAMELS simulations to model the surface brightness maps of the OVII and OVIII ion lines and compute summary statistics like photon counts and 2-point correlation functions to infer the properties of the WHIM. Our findings confirm that detectable WHIM emission is primarily associated with galaxy haloes, and the properties of the WHIM show minimal evolution from $z \sim 0.5$ to the present time. By exploring a wide range of parameters within the CAMELS suite, we investigate the sensitivity of WHIM properties to cosmology and energy feedback mechanisms influenced by active galactic nuclei and stellar activity. This approach allows us to separate the cosmological aspects from the baryonic processes and place constraints on the latter. Additionally, we provide forecasts for WHIM observations using a spectrometer similar to X-IFU. We anticipate detecting 1–3 WHIM emission lines per pixel and mapping the WHIM emission profile around haloes up to a few tens of arcminutes, surpassing the typical size of a WHIM emitter. Overall, our work demonstrates the potential of emission studies to probe the densest phase of the WHIM, shedding light on its physical properties and offering insights into the cosmological and baryonic processes at play.

Key words: methods: numerical – galaxies: evolution – intergalactic medium – large-scale structure of Universe – cosmology: theory.

1 INTRODUCTION

The observed abundance, in the spectra of distant quasars, of the light elements produced during the big bang nucleosynthesis has provided us with a spectacular and precise estimate of the comoving abundance of baryonic matter in the Universe (Cyburt et al. 2016) at that epoch. A measurement that is in very good agreement with the estimate of the baryon abundance at the epoch of the matter–radiation decoupling obtained by analysing the angular spectrum of the temperature fluctuations in the cosmic microwave background (Planck Collaboration 2020). The discovery that, instead, about half of the expected baryons are missing from the observed total mass budget in the local Universe came as a surprise and constitutes what has been dubbed the 'Missing Baryons' problem ever since (Fukugita, Hogan & Peebles 1998; Cen & Ostriker 1999a). More recent observations confirm that the problem is still there and that, despite dedicated searches, about 30 per cent of the baryons in the

local Universe still evade detection (Shull, Smith & Danforth 2012). Finally, a third, new method for estimating the baryon density that exploits the properties of the Fast Radio Bursts has been proposed and applied to existing data (Macquart et al. 2020). The results provide an estimate of the mean baryon density that is in good agreement with independent estimates.

Hydrodynamic simulations designed to follow the evolution of cosmic structures in large regions of a ΛCDM Universe (Cen & Ostriker 1999a) have indicated the solution to the problem: a sizable fraction of baryons in the low-redshift Universe is in a gaseous form and traces the large-scale filaments and the external regions of the dense knots that constitute the cosmic web. This gas is shock-heated and ionized during the buildup of the large-scale cosmic structures. As a result, most baryons are now expected to be in the form of a highly ionized, warm-hot diffuse gas with temperatures in the range $T \sim 10^5 - 10^7$ K and number densities of $n \sim 10^{-6} - 10^{-4}$ cm^{-3}: the 'warm-hot intergalactic medium' (WHIM). Because of its physical state, it is very hard to detect, since its high ionization state leaves no signature in the local Lyman-α forest and because of its low density its bremsstrahlung emission is to faint to be detected in the X-ray

*E-mail: g.parimbelli90@gmail.com

continuum. One of the best strategies to detect the missing baryons is, instead, to observe the characteristic absorption or emission lines in the X-ray band of the highly ionized 'metals' produced in the stars and then diffused in the intergalactic medium by galactic winds and supernovae explosions.

Since detecting absorption lines in the spectra of bright background X-ray sources offers higher sensitivity than observing the WHIM lines in emission, most of the theoretical studies (e.g. Viel et al. 2003, 2005; Cen & Fang 2006; Branchini et al. 2009; Tepper-García et al. 2011; Cen 2012; Shull et al. 2012; Oppenheimer et al. 2016, 2018; Rahmati et al. 2016; Nelson et al. 2018b; Martizzi et al. 2019; Wijers et al. 2019) and observational efforts (see e.g. Nicastro et al. 2017 and references therein) have been focusing on this possibility. This strategy proved to be successful and eventually led to the unambiguous detections of the WHIM in the X-ray spectra of two bright quasars (Nicastro et al. 2018; Kovács et al. 2019).

These important discoveries have validated the WHIM model that has been built from the hydrodynamic simulations and, more in general, have confirmed the correctness of the cosmological structure formation model in the ΛCDM framework. However, the paucity of the WHIM line detections and the very nature of the absorption studies that only allows one to probe the WHIM along a few, pre-selected directions, makes it difficult to probe the physical status and spatial distributions of a large fraction of the cosmic baryons in the low-redshift Universe.

Studying the WHIM in emission could, in principle, significantly improve our knowledge of the missing baryons physics for several reasons. First of all, the use of integral field spectroscopy allows one to probe the distribution of the missing baryons over any volume, and not just along the sightlines to bright sources. The technique is similar to that of the line emission mapping with the 21 cm line in the radio band, as well as it can be performed in the optical (e.g. Stark et al. 2021) and in infrared (e.g. Treu et al. 2022), except that in this case one should use the metal lines in the soft X-ray band. Furthermore, absorption and emission line studies are highly complementary. Absorption is proportional to the local density of the gas and preferentially occurs in in regions of moderate overdensity. On the contrary, the emission signal is approximately proportional to the square of the density and, therefore, preferentially produced in high density environments, more sensitive to stellar feedback and AGN activity.

What hampered emission studies so far is the difficulty to disentangle the WHIM signal from foreground emission, which is typically dominant. As a result, only a few, somewhat controversial, claims of WHIM detection in emission have been made (i.e. Nicastro et al. 2005; Zappacosta et al. 2005; Werner et al. 2008; Bonamente et al. 2022) and turned out to be produced by gas with density and temperature higher than the typical WHIM and associated with the external parts of virialized objects, like galaxy clusters. As a result, a comparatively smaller number of studies have been dedicated to modelling the WHIM in emission using hydrodynamic simulations (Cen & Fang 2006; Bertone et al. 2010; Takei et al. 2011; Ursino et al. 2011; Cen 2012; Roncarelli et al. 2012; Nelson et al. 2018b) and even less have contemplated the possibility to combine absorption and emission studies (e.g. Branchini et al. (2009)). The sensitivity of the X-ray emission lines to the local gas density makes them an ideal probe to the circumgalactic medium (CGM hereafter) associated with the extended galaxy haloes. CGM has been recognized as a major reservoir of the missing baryons, along with the Intergalactic medium not associated with virialized structures. Its proximity with galaxies makes the CGM sensitive to the complex energy feedback processes and justifies the interest in its theoretical modelling (i.e.

Truong et al. (2020); Wijers, Schaye & Oppenheimer (2020); Truong et al. (2021); Wijers & Schaye (2022)) and their comparison with X-ray observations (Chadayammuri et al. 2022; Comparat et al. 2022). On the other hand the definitions of WHIM and CGM are somewhat arbitrary (and certainly not unique in the literature) which makes their separation rather blurred. For this reason in this work we shall use the term WHIM for all line emitting gas in a given temperature and density range, whether or not it is associated with virialized structures. We will make no attempt to specifically isolate the CGM contribution except in Section 4.6 in which we will estimate 1-point statistics of the line counts generated by the emitting gas within virialized haloes.

The approaching of the new era of integral field spectroscopy in the X-ray band with the planned XRISM and Athena space missions (Nandra et al. 2013; XRISM Science Team 2020), as well as the Line Emission Mapper Probe concept[1] (Kraft et al. 2022), has triggered a renewed interest in the subject that justifies a fresher and deeper look into the subject. A significant update of the previous studies, which constitutes the main goal of this paper, is made possible thanks to the availability of a new, publicly available, large set of state-of-the-art hydrodynamic simulations, the CAMELS suite (Villaescusa-Navarro et al. 2020, 2022). These simulations allow us to overcome one potential issue of the previous analysis: the fact that predictions of the WHIM emission properties were based on a single or a handful of numerical experiments, while we know that theoretical uncertainty significantly contribute, and possibly dominate, the error budget. Thanks to the CAMELS suite in this work we will be able to span the large space of the parameters that drive the evolution of the mass density field and that regulate the energy feedback processes. Moreover, thanks to the presence of two different sets of simulations performed with two different hydrodynamic codes, AREPO (Weinberger, Springel & Pakmor 2019) and GIZMO (Hopkins 2015), we will be able to appreciate the sensitivity to the numerical technique used to simulate the WHIM.

We aim at understanding the properties of the WHIM in emission through the common summary statistics that will be computed from the X-ray surface brightness maps generated by integral field spectroscopy, namely the number counts of the characteristics WHIM emission line (and for the sake of simplicity we will focus on the most prominent ones: on the OVII line triplet with rest frame energies $E_{OVII} = 0.56098, 0.56874, 0.57395$ keV and the OVIII singlet at $E_{OVIII} = 0.65355$ keV) and the angular 2-point correlation function of these lines and their cross-correlation with galaxies (and their halo host). For this we will need to specify the characteristics of the detector.

Here we assume that observations will be performed with a calorimeter-based spectrometer whose technical specifications match those originally proposed for the X-IFU instrument that should have been placed on board of the Athena satellite (see Nandra et al. (2013)). We maintain this assumption despite the fact that, while this work was completed, the Athena satellite and its instrument have undergone a re-definition exercise. The reason for this is that our goal is not to optimize detectors' characteristics to the WHIM science case or to provide forecasts to specific instrument configurations. Instead, we aim at providing realistic, rather than specific, predictions for the summary statistics that could be estimated with an X-ray imaging spectrometer suitable to, rather than optimized for, WHIM-oriented studies.

---

[1] https://lem.physics.wisc.edu

Table 1. The table describes the specifics of the 10 snapshots we consider in our analysis. The first column reports the redshifts of the snapshots. The other columns report the comoving distance to the redshift, the size of the grid employed to build the maps, the thickness of the slice corresponding to the spatial resolution along the line-of-sight and the field of view that the simulation represents, respectively.All these quantities have been computed using the fiducial cosmology of the CV subsets.

z	Comoving distance $D_L(z)$ [Mpc/h]	Grid size N_{grid}	Slice thickness ΔL [Mpc/h]	Field of view FoV [deg^2]
0.54	2163.0	732	14.4	1.0
0.47	1822.8	829	14.3	1.3
0.40	1508.9	955	14.2	1.8
0.33	1223.1	1123	14.0	2.4
0.27	963.0	1360	13.8	3.6
0.21	727.3	1716	13.6	5.7
0.15	514.6	2313	13.4	10.3
0.10	323.3	3509	13.1	23.8
0.05	152.3	7104	12.8	97.4
0.04	123.6	8679	12.8	145.3

This paper is organized as follows. In Section 2 we present the subset simulations that we have selected from the CAMELS suite and that we use in our analysis, discussing the criteria for this choice. In Section 3 we describe the procedure adopted to generate the simulated X-ray emission maps from the hydrodynamic simulation outputs. Some simplifying assumptions have been made in the process that we discuss here. In this section we also describe the estimator used to compute the summary statistics considered in this work. In Section 4 we present the results of our analysis and test their robustness to various physical and numerical effects. In Section 5 we provide some forecast on the WHIM line detectability and compare our results with those of Takei et al. (2011). Finally, in Section 6 we discuss our results and draw our conclusions.

2 DATA SETS

In this section we describe the simulated data sets that we use in this work to generate dark matter halo catalogues, mock WHIM spectra, and surface brightness maps.

2.1 The CAMELS Parent Data set

The parent data set is the CAMELS suite of cosmological simulations (Villaescusa-Navarro et al. 2020) which consists of 4233 simulations, about half of which are dark-matter-only and half (magneto)-hydrodynamic, designed to train machine learning techniques and applications to astrophysical data sets. The simulations follow the evolution of cosmic structures from $z = 127$ to present day using 256^3 dark matter (DM) particles as well as, when present, 256^3 fluid particles in a cubic box of 25 comoving Mpc/h. All simulations assume a ΛCDM model. For each realization, 34 snapshots are created at various redshifts. Since we are interested in studying the WHIM which is a relatively local phenomenon, we only use the ten snapshots at $z \leq 0.54$ whose characteristics are specified in Table 1. To avoid divergence when creating the flux maps used in this work we place the $z = 0$ snapshot at a distance of $\sim$118 Mpc/h (the precise value depending on the cosmology assumed) from the observer, corresponding to $z = 0.04$.

The suite is designed to span a wide region of a 6D parameter space. Two dimensions are meant to explore different cosmological

models, characterized by the mean matter density Ω_m and the clustering amplitude σ_8. The remaining 4 dimensions are meant to sample different energy feedback models. Two of them regulate the stellar feedback from supernovae (parameter A_{SN1}) and from galactic wind (A_{SN2}). The other two parametrize AGN feedback through energy-momentum injection (A_{AGN1}) and and jet speed (A_{AGN2}). These parameters measure the relative variations with respect to the reference feedback models used in the IllustrisTNG and SIMBA simulations (Davé et al. 2019; Nelson et al. 2019; Villaescusa-Navarro et al. 2020). Their values are normalized accordingly.

In this work we also use catalogues of DM haloes with masses in the range $\sim 4 \times 10^8 - 5 \times 10^{13} M_\odot/h$ that have been identified using the friends-of-friends algorithm (Huchra & Geller 1982; Davis et al. 1985) and the SUBFIND software (Springel et al. 2001).

All cosmological parameters but σ_8 and Ω_m are kept fixed in the analysis. They are: $\Omega_b = 0.049$, $h = 0.6711$, $n_s = 0.9624$. The value of Ω_b implies an initial mass of $1.27 \times 10^7 M_\odot/h$ for the gas particles.

The CAMELS suite includes two types of hydrodynamic simulations, that we use in this work:

(i) **IllustrisTNG**: These are 1092 hydrodynamic simulations run with the AREPO code (Springel 2010; Weinberger et al. 2019) that implements the same galaxy formation model and subgrid physics as the original IllustrisTNG simulations of Weinberger et al. (2017); Pillepich et al. (2018); Nelson et al. (2019)

(ii) **SIMBA**: This is a matching set of 1092 hydrodynamic simulations run with the GIZMO code (Hopkins 2015) that implements the same galaxy formation model and subgrid physics as the original SIMBA simulations of Davé et al. (2019).

2.2 Data sets used in this work

Each data set described above is a suite of simulations from which we selected a few for our purposes. The subset of simulations used in this work consists of the following samples:

(i) **IllustrisTNG-CV** and **SIMBA-CV** samples. These are 27 + 27 simulations extracted from both the **IllustrisTNG** and the **SIMBA** suites. All of them use the same set of cosmological and astrophysical parameters but different random seeds to set initial conditions. The relevant parameters that characterize these samples, which we regard as the set of fiducial parameters, are listed in Table 2. The results obtained from this samples will allow us to evaluate the effect of the cosmic variance and to estimate its contribution to the total error budget.

(ii) **IllustrisTNG-LH**. This set consists of 1000 realizations selected from the **IllustrisTNG** sample. These simulations have been evolved from different initial conditions and by using different values for the 6 free parameters (of both cosmological and astrophysical type) chosen within a pre-defined range around the fiducial values. The resulting 6D parameter space is very wide, since it was designed for machine learning purposes. However, in this work we are interested in studying the properties of the WHIM in a realistic cosmological setup that matches observations. Therefore, we decided to explore a limited region of the parameter space in which *i)* the value of Ω_m is consistent with the results of the 3x2pt joint weak lensing and clustering analyses of the DES-year 3 catalogue (DES Collaboration et al. 2021) and *ii)* the value of σ_8 is consistent with those obtained by the Planck Team (Planck Collaboration 2020). As a result we consider Ω_m and σ_8 values in the ranges [0.25,0.35] and [0.75,0.85], respectively. Once these selections criteria are applied we are left with 63 simulations that we use to evaluate the uncertainties in predicting

Table 2. Subsets of CAMELS simulations used in this work. Column 1: Set name. Column 2: Number of simulations. Column 3: Random seed(s) used to set the initial conditions. Column 4: σ_8 range of values. Column 5: Ω_m range of values. Column 6: A_{SN1} and A_{AGN1} range of values. The two parameters are set equal. Column 7: A_{SN2} and A_{AGN2} range of values. The two parameters are set equal.

Name	N. realizations	random seeds	Ω_m	σ_8	A_{SN1}, A_{AGN1}	A_{SN2}, A_{AGN2}
IllustrisTNG-CV	27	Several	0.3	0.8	1	1
SIMBA-CV	27	Several	0.3	0.8	1	1
IllustrisTNG-LH	63	Several	[0.25, 0.35]	[0.75, 0.85]	[0.25, 4]	[0.5, 2]
IllustrisTNG-1P	45	Same	[0.25, 0.35]	[0.75, 0.85]	[0.25, 4]	[0.5, 2]
TNG300	1		0.3089	0.8159	1	1
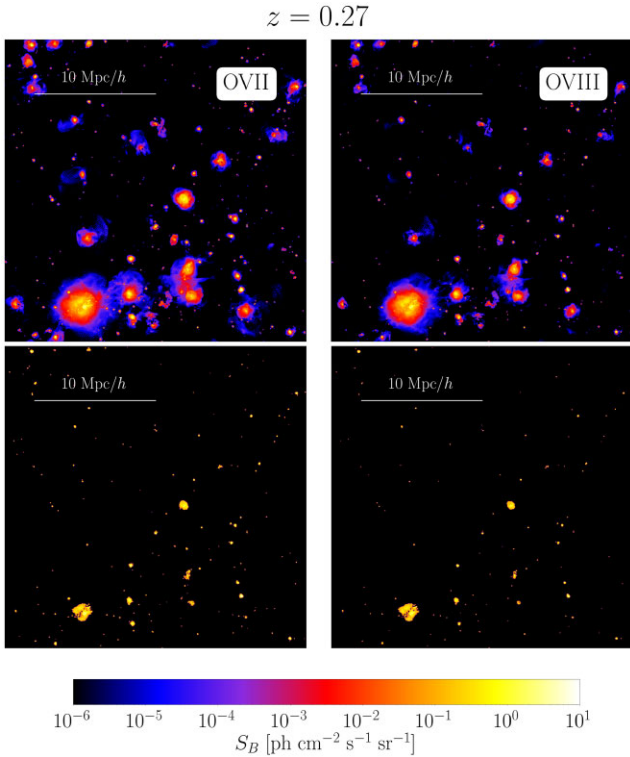
$$z = 0.27$$

Figure 1. Surface brightness maps of the OVII (left) and OVIII (right) emission lines from the gas in slice 13.8 Mpc/h thick and 25 Mpc/h wide extracted from the $z = 0.27$ snapshot of the IllustrisTNG-1P simulation with the parameters of the fiducial cosmological model adopted in this work. Top panels: emission from the WHIM gas particles. Bottom panels: only pixels brighter than 0.1 ph cm^{-2} s^{-1} sr^{-1}, corresponding to a 3-σ detection threshold with a 100 ks Athena X-IFU observation are shown.

the WHIM properties, including uncertainties in modelling stellar and AGN feedback mechanisms.

(iii) **IllustrisTNG-1P** : The simulations in this subset have been performed varying one parameter at the time and using the same initial conditions. 11 different values are used for each of the 6 parameters, totaling to 61 simulations. We consider only the parameters whose values are in the same range as in the **IllustrisTNG-LH** sample, for a total 45 simulations.

In this work we consider an additional data set which is not part of the CAMELS suite: the **TNG300** hydrodynamic simulation (Marinacci et al. 2018; Naiman et al. 2018; Pillepich et al. 2018; Springel et al. 2018; Nelson et al. 2018a, 2019). This is a single numerical experiment performed in a box of side 205 comoving Mpc/h, i.e. ~ 8 times larger than the CAMELS one, that assumes a Planck Collaboration 2016) flat ΛCDM cosmology with $\Omega_m =$

0.3089, $\Omega_b = 0.0486$, $h = 0.6774$, $n_s = 0.9667$, $\sigma_8 = 0.8159$. We use this simulation to assess the effects of the large wavelength modes, that are missing from the CAMELS data set, and of the mass resolution, which is higher in this case because the number of particles in this simulation is about 1000 larger than in the CAMELS (the mass of a single gas particle is $7.6 \times 10^6 \, M_\odot/h$). Moreover, performing the analysis in a volume ~ 550 times larger than that of the CAMELS will allow us to better samples rare events associated with very massive haloes and, in general, to improve statistics.

3 MODELLING THE WHIM PROPERTIES

We now use the hydrodynamic simulations to model the OVII and OVIII line emission maps (Section 3.1) and to compute summary statistics such as emission line counts and 2-point angular correlation (Section 3.2).

3.1 Line surface brightness maps

The WHIM X-ray spectrum is characterized by the emission (or absorption) lines of several highly ionized 'metals' such as carbon, oxygen, neon, iron and magnesium. Here we will focus on the most prominent line systems: the OVII triplet at 0.561, 0.569, 0.574 keV and the OVIII singlet at 0.653 keV. To model the X-ray emission spectra from the simulation outputs we proceed as follows:

(i) We divide the gas particles in the simulations in two subsets: the WHIM and non WHIM particles. WHIM particles have gas overdensity $\delta < 1,000$ and temperature $10^5 \, K < T < 10^7 \, K$. All remaining particles constitute the non-WHIM gas. The definition is somewhat arbitrary but matches that used in several works in the literature (Takei et al. 2011; Roncarelli et al. 2012).

(ii) For each gas particle, WHIM and non-WHIM, we compute the emissivity spectra by feeding density, temperature and metallicity of the gas particle to the pyXSIM code (ZuHone & Hallman 2016). To express the absolute metallicity of the gas into solar units we used the tables in Asplund et al. (2009). In the pyXSIM code the OVII and OVIII ion fractions are computed assuming collisional ionization equilibrium using the AtomDB tables and APEC emission model (Smith et al. 2001; Foster et al. 2012), i.e. we ignore photo-ionization. This assumption, which has been adopted in most of the previous emission studies of the WHIM (Takei et al. 2011; Roncarelli et al. 2012), is satisfied at low redshifts for hydrogen gas density $n_H > 10^{-4}$ (see e.g. Fig. 3 of Nelson et al. (2018b)). Since the OVII and OVIII line emissivity approximately scales as n_H^2 (see e.g. Fig. 1 of Bertone et al. (2010)) the line surface brightness, especially the one potentially detectable by future experiments, is dominated by the signal generated in regions where the gas density is close to virial, where the conditions for collisional ionization equilibrium hold true.

(iii) Once the emission spectrum for each particle is computed, we estimate the OVII and OVIII line emissivity $j(\rho, T, Z)$ by estimating

Table 3. Specific of the Athena X-IFU instrument (Nandra et al. 2013).

X-IFU specifics	
Angular resolution	$\theta_{\text{res}} = 5''$
Energy resolution	$\Delta E = 2.5$ eV
Detection threshold	$S_{\text{B, min}} = 0.1$ ph cm^{-2} s^{-1} sr^{-1}
($t_{\text{obs}} = 100$ ks)	
Field of view	$(5$ arcmin$)^2$

the energy contributed by a portion of the spectrum centered around the emission line and slightly larger than the width of the line.

(iv) We then compute the photon flux of the oxygen lines from each gas element as Bertone et al. (2010):

$$\Phi_{\text{ph}} = \frac{j(\rho, T, Z)}{4\pi D_L^2(z)} \frac{m}{\rho} \frac{1+z}{\langle E \rangle}, \tag{1}$$

where m is the mass of the gas particle at the observed redshift z and luminosity distance $D_L(z)$, ρ is the gas density and $<E>$ is the mean rest frame energy in the spectral range considered.

(v) The OVII and OVIII line fluxes of all particles are then interpolated on a grid, summed over and divided by the solid angle subtended by the pixel to obtain the OVII and OVIII surface brightness maps.

The final map consists of a 3D data cube in which each pixel specified the OVII and OVIII surface brightness at a given angular position and contributed by the gas at a given redshift. Similar 3D data cubes will be generated by calorimeters on board of next generation X-ray satellite, designed to perform spatially resolved spectroscopy. Therefore, to add a realistic touch to our results, we decided to set the size of the 3D pixels by matching the expected angular resolution θ_{res} and energy resolution ΔE of the X-IFU detector that is expected to fly on board of Athena (Nandra et al. 2013). Their values are listed in Table 3. We notice that the angular size of the pixel (5'), is smaller than the typical angular size of a few arcminutes of the typical WHIM emitter (Takei et al. 2011), potentially allowing one to probe the spatial and the clustering properties of the WHIM (that we model in Section 4.3 and 4.4) and to efficiently remove point-like X-ray sources, like AGNs, that otherwise would artificially enhance the noise level.

The angular resolution sets the mesh size of the grid which, at the redshift of the output z, determines the number of grid points

$$N_{\text{grid}}^3 = \text{int} \left(\frac{L}{\theta_{\text{res}} \, \chi(z)} \right)^3, \tag{2}$$

where L is the box size and $\chi(z)$ is the comoving distance to redshift z in the assumed cosmology.

The energy resolution sets the thickness of each slice of the data cube along the line of sight direction. For simplicity we assume the distant observer approximation, i.e. the same line of sight to all pixels in the grid. Given the small size of the simulation boxes this assumption is justified for all but the smallest redshift snapshots. For a line emission with rest-frame energy E the thickness ΔL is:

$$\Delta L = \frac{\Delta E}{E} (1+z) \frac{c}{H(z)}, \tag{3}$$

where $H(z)$ is the Hubble constant at the redshift of the snapshot z. This is the thickness of the surface brightness maps, i.e. each map is obtained by integrating along each line of sight the line flux at the positions of all gridpoints within ΔL.

Since we are interested in two lines, OVII and OVIII, but would like to use the same thickness for both emission maps, we set $E = 0.6$ keV,

i.e. the average of the OVII and OVIII emission line energies. The area subtended by the computational cube, which represents the field of view of the map, and its thickness depends on the cosmological model adopted line each simulations and, of course, on the redshift of the snapshot. However, the dependence on the cosmology is rather mild for two reasons. The first one is that we restrict our analysis to the low-redshift Universe. The second one is that the range of σ_8 and Ω_m values in the simulations used in our analysis is quite limited. Therefore, in our analysis we ignore the dependence on the cosmology and assume that the field of view and depth of all surface brightness maps are identical and equal to that of the fiducial cosmological models. Their values are listed in Table 1. We further notice that detectors with an energy resolution of a few eV will produce brightness maps of substantial thickness, comparable to the size of the simulation boxes. As a result, our surface brightness maps are meant to represents the ideal case in which the observations come from a specific redshift, corresponding to that of the simulation snapshots, but fail to reproduce the whole 3D complexity of an actual datacube, for which the simulated emission from the whole light-cone should be generated.

3.2 Summary statistics

Surface brightness maps generated by the integral field units contain a wealth of information that needs to be efficiently compressed. Two summary statistics that are widely used and that we consider in this work are

(i) the $\log N - \log S_B$, i.e. the number of detected emission or the 1-point probability distribution of the pixel counts as a function of the line surface brightness, S_B.

(ii) the angular 2-point correlation function, $w(\theta)$, of the line surface brightness in two pixels separated by an angle θ.

Angular cross-correlation can also be estimated if the angular position of other extragalactic sources in the same region is also available. One such example is the angular cross-correlation between the line surface brightness and the galaxies.

To characterize the WHIM properties in our simulated maps we use these statistical tools. For the latter, i.e. the angular cross-correlation, we consider the dark matter haloes extracted from the simulations to avoid the complication of the galaxy–halo relation in the simulated data.

Projection effects related induced by the energy resolution of the integral field units makes it impossible to probe the spatial distribution of the line emitting gas along the sight line. Which, however, is accessible in the simulation box. Therefore, we decided to also estimate the 2-point correlation function of the 3D surface brightness fields in the simulation as well as the cross-correlation between halo number density and the surface brightness fields. This quantity, that cannot be observed with currently proposed integral field units, is nevertheless useful to study the spatial distribution of the WHIM. Moreover, since in these maps the redshift of the emission line is used as a proxy to the distance of the emitter, the estimate of this 2-point correlation function is affected by the so-called redshift distortions, i.e. from the anisotropy induced by the peculiar velocity of the emitting gas with respect to the Hubble flow (Kaiser 1987; Hamilton 1998). Anisotropic correlation functions are characterized by nonzero quadrupole and hexadecapole moments that can be measured and used to investigate the dynamics of the line emitting gas. For this reason, for the 3D fields, we estimate both the monopole and the quadrupole moments of the correlation function.

To summarize, the statistical quantities that we use in this work are:

(i) The oxygen line emitters counts $\log N - \log S_B$. To estimate this quantity we simply count the number of pixels, in the line surface brightness maps, with a surface brightness level larger than S_B. This way we estimate the cumulative probability distribution of the OVII and OVIII line emitters. We also estimate the same quantity for both emitters, OVII and OVIII, by considering the pixels in which the OVII and OVIII surface brightness are both larger than S_B. This quantity is estimated at different redshifts using all available snapshots. Moreover, we compare our results with those of Takei et al. (2011) and Roncarelli et al. (2012). In their case, however, the $\log N - \log S_B$ statistics is estimated considering a full light-cone to $z = 0.54$ and considering angular resolutions of a few arcminutes, i.e. over larger pixels. The procedure used to build a similar light-cone and to reduce the angular resolution of our maps is described in details in Section 5.

(ii) The monopole and quadrupole moments of the spatial 2-point autocorrelation function $\xi(\mathbf{r})$ of the OVII and OVIII surface brightness at the points of a cubic grid. Here we ignore the effect of the energy resolution of the detector and estimate the 3D correlation on the $N_{\rm grid}^3$ points of the grid, where the value of the $N_{\rm grid}$ is specified in Table 2. Since we are using computational boxes that assume periodic boundary conditions we use the estimator proposed by Taruya et al. (2009) as implemented in the PYLIANS3 package. Input to this estimator is the fluctuation of the line surface brightness with respect to the mean, specified on a cubic grid $\delta(\mathbf{x})$. The field is Fourier transformed, its Fourier coefficients $\delta(\mathbf{k})$ squared, and the result transformed back. The quadrupole moment is estimated by weighting the cubic grid for $5/2\,\mathcal{L}_2(\mu)$, where $\mathcal{L}_2$ is the 2nd-order Legendre polynomial and μ is the cosine angle between the line-of-sight and the wavelength vector $\mathbf{k}$, before averaging over all pixel pairs.

The spatial 2-point correlation functions are estimated at the redshifts of the simulations' snapshots, for the various fluctuations field defined on cubic grids. The number of gridpoints is set by the X-IFU angular resolution and, as shown in Table 1, is very large. Estimating the 2-point correlations using so many points would be computationally prohibitive and not very informative, since it would probe scales smaller than the typical halo size. Therefore, for the spatial 2-point correlation functions, we decided to re-bin the fluctuation fields on a coarser grid of 512^3 points, corresponding to a spatial resolution of 49 kpc/h; a scale comparable to the size of a Milky Way sized halo.

(iii) The monopole and quadrupole moments of the spatial 2-point cross-correlation function of the oxygen line surface brightness and the halo counts. The procedure is similar to that of the autocorrelation except for the fact that now two fields are used, one of which is obtained by interpolating the halo number counts at the positions of the 512^3 cubic grid, and that both are fed into the Taruya estimator.

(iv) The angular auto- and cross-correlation function of the line emitters and dark matter haloes, $w(\theta)$. Also in this case the procedure to estimate this quantity is similar to the one used to compute $\xi(\mathbf{r})$ except for the fact that now the fluctuations fields are specified at the point of a square, rather than cubic, grid.

4 RESULTS

In this section we present the main results of our analysis. First of all, we visually inspect the OVII and OVIII surface brightness maps obtained at different redshifts and for different choices of Ω_m

and σ_8 parameters and energy feedback models. We compute the $\log N - \log S_B$ statistics statistics of these maps and evaluate their uncertainty. Then we use the full simulation boxes to measure the spatial 2-point correlation functions of the oxygen emitters and their cross-correlation with the dark matter haloes. Finally, we estimate the angular auto- and cross- 2-point correlation functions of the above quantities from using the 2D surface brightness maps with energy and angular resolution matching these of the X-IFU detector.

4.1 Surface brightness maps

Fig. 1 shows the OVII (top left panel) and OVIII (top right) surface brightness maps of the redshift slice corresponding to the $z = 0.27$ snapshot of the IllustrisTNG-1P simulation. The parameters of the emison model are the same as the fiducial ones used in the SIMBA-CV and IllustrisTNG-CV sets. We use the IllustrisTNG-1P simulations, which have the same initial conditions, to assess the sensitivity to the choice of cosmological parameters and energy feedback models free of cosmic variance. We first show the $z = 0.27$ case since it roughly corresponds to the mean redshift in the range we have considered. The IllustrisTNG-1P realization contains one massive halo of $M \sim 9 \times 10^{13}\,M_\odot/h$, that features prominently in the bottom left part of the map, and a rather large void. The presence of both structures is quite unlikely in a box of 25 Mpc/h randomly placed in the Universe. As a result, the simulated properties of the WHIM in this box are not representative of the cosmic mean. We shall address this issue in the next sections, in which we quantify the impact of the cosmic variance on the summary statistics. Here, however, we are interested in qualitatively comparing the *relative* differences among different WHIM models, which requires using the same realization, however unlikely this may be.

The surface brightness levels are colour-coded according to the reference bar shown at the bottom of the plot. In the OVIII maps the emission is more concentrated near the center of the haloes whereas the OVII has a larger angular extension. This is expected since the gas temperature and density are more favourable to OVIII ions.

These maps do not trace the spatial distribution of the oxygen ions along the large-scale filaments which, instead, can be seen when plotting the column density of these ions, as in Fig. 1 of Nelson et al. (2018b) or Fig. 2 of Wijers et al. (2019).

A more direct comparison can be made with the emission maps of Bertone et al. (2010), obtained from the OWLS simulations. They look qualitatively similar to ours in the high density regions centered on massive haloes ($M \gtrsim 10^{12}\,M_\odot/h$). However, the diffuse emission from low density filaments seen in theri maps is largely missing from ours. This difference likely result from having assumed collisional ionization equilibrium: a valid hypothesis in high density and temperature environments that, however, underestimate the OVII and OVIII ionization fraction in low density regions. However, it is a good approximation for gas in the high density regions that generate a line surface brightness signal above 0.1 photons cm^{-2} s^{-1} sr^{-1} (corresponding to a 3-σ detection threshold for a 100 ks observations with Athena X-IFU according to Takei et al. (2011); Kaastra et al. (2013)) which we show in the two bottom panels. This gas is mostly associated with dark matter haloes, whereas weaker emission from halo outskirts could only be detected indirectly via stacking technique or through cross-correlation analyses with the spatial distribution of galaxies.

The evolution of the line surface brightness as a function of time can be appreciated in Fig. 2, where we show the same OVII map at $z = 0.27$ as in Fig. 1 next to the maps at obtained from the $z = 0.54$ (left) and $z = 0.04$ (right) snapshots. Line emission is always
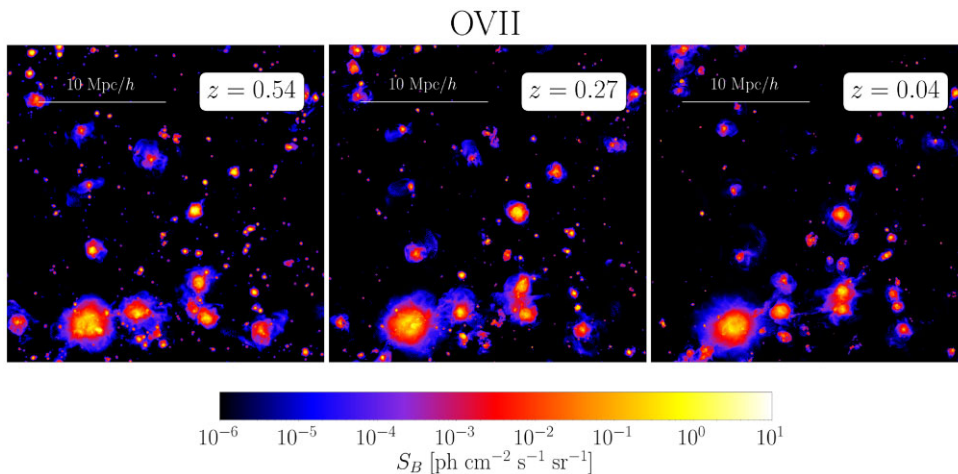
OVII

Figure 2. OVII line surface brightness maps of the same region as Fig. 1 seen at three different redshifts: $z = 0.54, 0.27, 0.04$ (from left to right). The thickness of the slide changes with redshift as indicated in Table 1.

associated with haloes and become progressively more concentrated around the massive ones as result of the merging process. We only show the OVII map since the redshift dependence of the OVIII map is very similar.

To explore the sensitivity of our results to the underlying cosmology, we have modified the two parameters that regulate the amplitude of the mass density fluctuations, σ_8, and the shape of the power spectrum along with the total mass content of the Universe, Ω_m. Both have been increased/decreased by the same amount, 0.04, with respect to the fiducial case. Increasing σ_8 and Ω_m enhances the clustering amplitude and the merging rate of the virialized structures which, in turns, extends the line surface brightness profile towards the outskirts of the haloes. The effect, however, is small and can be barely in the simulated brightness maps that, for this reason, are not shown here. The lack of sensitivity of the line emission signal, especially the one potentially detectable by future X-ray experiments, is remarkable. Especially when compared with the impact of the feedback energy processes.

The effect of varying the four parameters that characterize the energy feedback models, illustrated in Fig. 3, is more spectacular. The four rows show the effect of increasing the parameters one by one, from left to right, with respect to the fiducial case shown in the central panels. The largest effect is obtained when changing the amount of energy injected through SN explosion (A_{SN1} parameter, top row) and the speed of the galactic winds (A_{SN2} parameter, second from the top). Increasing both effects significantly enhances the surface brightness in halo surroundings without dimming that in the center. The fact that increasing the amount of energy injected increases the line emissivity of the intergalactic medium is not surprising and confirms the results of Roncarelli et al. (2012) whom, however, used a different hydrodynamic simulation and energy feedback criteria.

The effect of energy feedback from AGNs, regulated by the two parameters A_{AGN1} and A_{AGN2}, shown in the two bottom rows, is comparatively less prominent. This behaviour is not unexpected. SNe go off in haloes of all masses while AGN feedback is more efficient in massive haloes, which are rare in the limited volume of the IllustrisTNG-CV simulations. As a result, the AGN feedback mechanism is typical subdominant in the CV set.

Due to the limited volume of the CV set, haloes more massive than $10^{13}\, M_\odot/h$ are rare, so that AGN feedback is important only for a minimal fraction of them. It also goes in the opposite direction:

increasing the energy release from AGN increases the surface brightness near the center of the haloes but decreases it in the outer parts. Finally, we notice that there must be a strong interplay among the different astrophysical parameters: for instance, increasing SN feedback will make it harder to create massive galaxies, i.e. the ones that are most likely to host an AGN; similarly, increasing AGN activity may release more energy and make SN explosions more or less efficient. The competing effect of these two energy release mechanisms on the OVII (but also OVIII) surface brightness is an interesting effect that we will quantify in the next section using summary statistics.

4.2 $\log N - \log S_B$ of the OVII and OVIII line emitters

To estimate the the $\log N - \log S_B$ statistics of the oxygen line emitters we count the number of pixels N in the maps above a given line surface brightness value, S_B. The results are shown in Fig. 4 for the OVII (left), OVIII (center) and for the joint OVII + OVIII (right) counts at three different redshifts ($z = 0.54, 0.27, 0.04$, from top to bottom). The results are shown in Fig. 4 for the OVII (left), OVIII (center) and for the joint OVII + OVIII (right) counts at three different redshifts ($z = 0.54, 0.27, 0.04$, from top to bottom). The curves show the counts averaged over the available 27 maps obtained from the IllustrisTNG-CV (cyan) and SIMBA-CV (red) simulations. The shaded areas of the same colour represent the standard deviation estimated from the *rms* scatter among the maps, all of them generated with the same set of WHIM model parameters. The broader grey band, plotted for the IllustrisTNG-CV case only to avoid overcrowding, shows the *rms* scatter estimated from the 63 IllustrisTNG-LH realizations characterized by different initial conditions and by different choices of the WHIM model parameters within the ranges ranges shown in Table 2. At small S_B values the error budget is dominated by cosmic variance since the blue and grey bands coincide. At large S_B values errors are dominated by model uncertainties, especially by those associated with the energy feedback models. Dashed curves show the $\log N - \log S_B$ curves of the oxygen lines generated by all the gas particles, not just the WHIM. Finally, a vertical line is drawn in correspondence to the reference surface brightness detection threshold 0.1 photons cm^{-2} s^{-1} sr^{-1}.

Perhaps the most interesting result is the systematic difference between the $\log N - \log S_B$ from the SIMBA and the IllustrisTNG
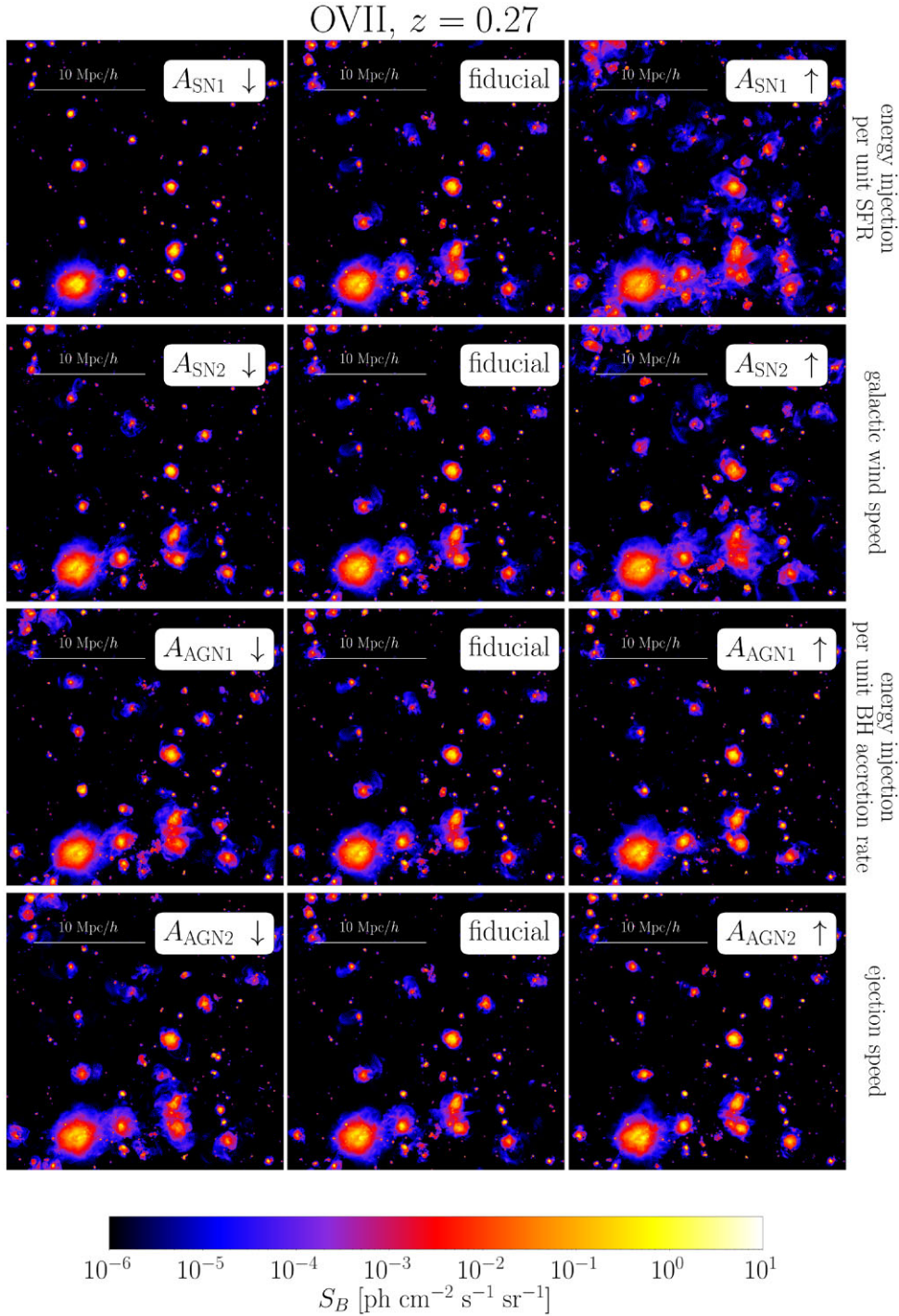
Figure 3. OVII line surface brightness maps of the same region as Fig. 1 from the $z = 0.27$ snapshot of IllustrisTNG-1P simulations that use different values of the parameters that regulate the energy feedback. The effect of increasing each one of the four parameters, specified in the white labels, from their minimum (left-hand panel) to the maximum (right) value, with respect to the fiducial case (center) is shown in each row.

maps. A difference in the simulations' outputs is to be expected. What is remarkable is the statistical significance of this difference which is of the same order as the statistical uncertainties quantified by the coloured bands. Therefore, differences in the techniques used to perform hydrodynamic represent a source of systematic errors that cannot be ignored in the total error budget. The SIMBA simulations systematically underestimate the number of WHIM emitters with respect to IllustrisTNG. This is also the case for the weak emission lines generated by the whole gas, but not for the strongest emitters, whose number is larger in the SIMBA case at low redshift. Another interesting feature is the similarity between the OVIII and OVIII + OVII curves, at all redshifts, for all type of gas particles and for both hydrodynamic experiments. In practice, the detection of an OVIII line almost guarantees that an OVII line is also observed, presumably from the same emitter, hence providing an unambiguous estimate of the emitter's redshift. For this reason, most
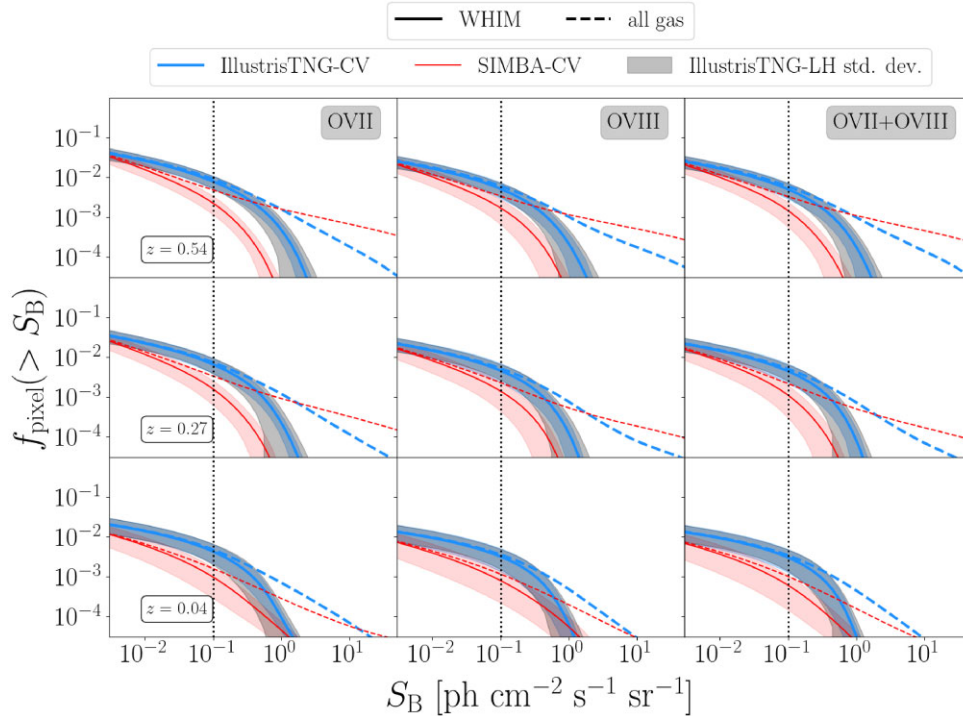
Figure 4. $\log N - \log S_B$ for OVII (left), OVIII (center) and OVII + OVIII (right) line counts in the brightness maps at three different redshifts: 0.54 (top), 0.27 (center) and 0.04 (bottom). In this and following figures we will always plot the *fraction*, rather than the total number, of pixels above a given S_B threshold, $f_{\text{pixel}}(> S_B)$. Cyan, thick, continuous curves and shaded area show the WHIM line counts averaged among the 27 IllustrisTNG-CV realizations and their *rms* scatter. Red, thin, continuous curves and shaded area show the same quantities for the SIMBA-CV case. Dashed curves of the same colours show the average line counts generated by all gas particles, including the WHIM. The grey band surrounding the IllustrisTNG-CV WHIM counts shows the *rms* scatter among the 63 IllustrisTNG-LH realizations. All the S_B left to the vertical dotted line at $0.1\,\text{ph}\,\text{cm}^{-2}\,\text{s}^{-1}\,\text{sr}^{-1}$ are below the 3-σ detection threshold in a 100 ks observation with Athena X-IFU.

often than not, we will only show the OVIII $\log N - \log S_B$ curves in the rest of the article. This result confirms that of Takei et al. (2011) based on yet another set of hydrodynamic simulations, although in their case the similarity between the OVIII and OVII + OVIII $\log N - \log S_B$ counts was less striking.

Finally, given the large number of pixels in the maps, N_{grid}^2, one expects that a large number of detections with Athena X-IFU are associated with the same physical structure. We shall return on this point and estimate the number of expected emitters per line-of-sight in Section 5.

The curves in Fig. 4 shows a characteristics break or knee that is qualitatively similar to that of the column density distribution function of the OVII and OVIII absorbers in the EAGLE and Illustris simulations (Wijers et al. 2019). This is not surprising since X-ray oxygen absorbers trace the bulk of the WHIM but avoid the hotter and denser regions where the strongest emission lines are generated. These lines are included in the counts that consider all gas particles, and not just the WHIM, represented by the dashed curves of of Fig. 4 that show no clear break.

Fig. 5 illustrates the sensitivity of the OVII and OVIII WHIM line counts to the four parameters that regulate the energy feedback. with respect to the fiducial case (represented, in each panel, by the continuous purple curve). We do consider the cosmological parameters since, as we have verified, the $\log N - \log S_B$ is remarkably robust to the choice of σ_8 and Ω_m in the interval we have considered. The shaded area represents the *rms* scatter among the 27 IllustrisTNG-CV realizations. We only show the $z = 0.27$ snapshots since the

qualitative dependence on the different parameters is the same at all redshifts. Dashed curves show the $\log N - \log S_B$ obtained when changing one parameter at the time, one in each row. Parameter's values are colour-coded and indicated in the vertical colour bar.

The effect of changing the energy feedback parameters is evident, as expected from the visual inspection of surface brightness maps in Fig. 3. The magnitude of the effect is illustrated in in Fig. 6 where we plot the residual line counts with respect to the fiducial case in units of the *rms* scatter.

The parameter that has the largest impact is the one that controls the energy injection from star formation processes. Increasing its value systematically increases the number emission lines with surface brightness as high as $\sim 1\,\text{ph}\,\text{cm}^{-2}\,\text{s}^{-1}\,\text{sr}^{-1}$ (and vice versa). The effect is (barely) larger than the expected variance for the 25 Mpc/h box. For brighter emitters the trend seems to be the opposite. The actual significance of this inversion, however, is questionable since in this very low number count regime the Gaussian hypothesis does not hold anymore, and the measured *rms* scatter is not sufficient to characterize the statistical significance of the event. The effect of the other three parameters is comparatively smaller and the trend less clear. Increasing the energy feedback from AGNs, regulated by the two parameters A_{AGN1} and A_{AGN2}, decreases the number of bright counts, hence confirming the qualitative analysis of the OVII surface brightness maps, though the variations are comparable to the cosmic variance.

The number WHIM counts drops to zero above $\sim 3\,\text{ph}\,\text{cm}^{-2}\,\text{s}^{-1}\,\text{sr}^{-1}$ makes it difficult to analyse the very
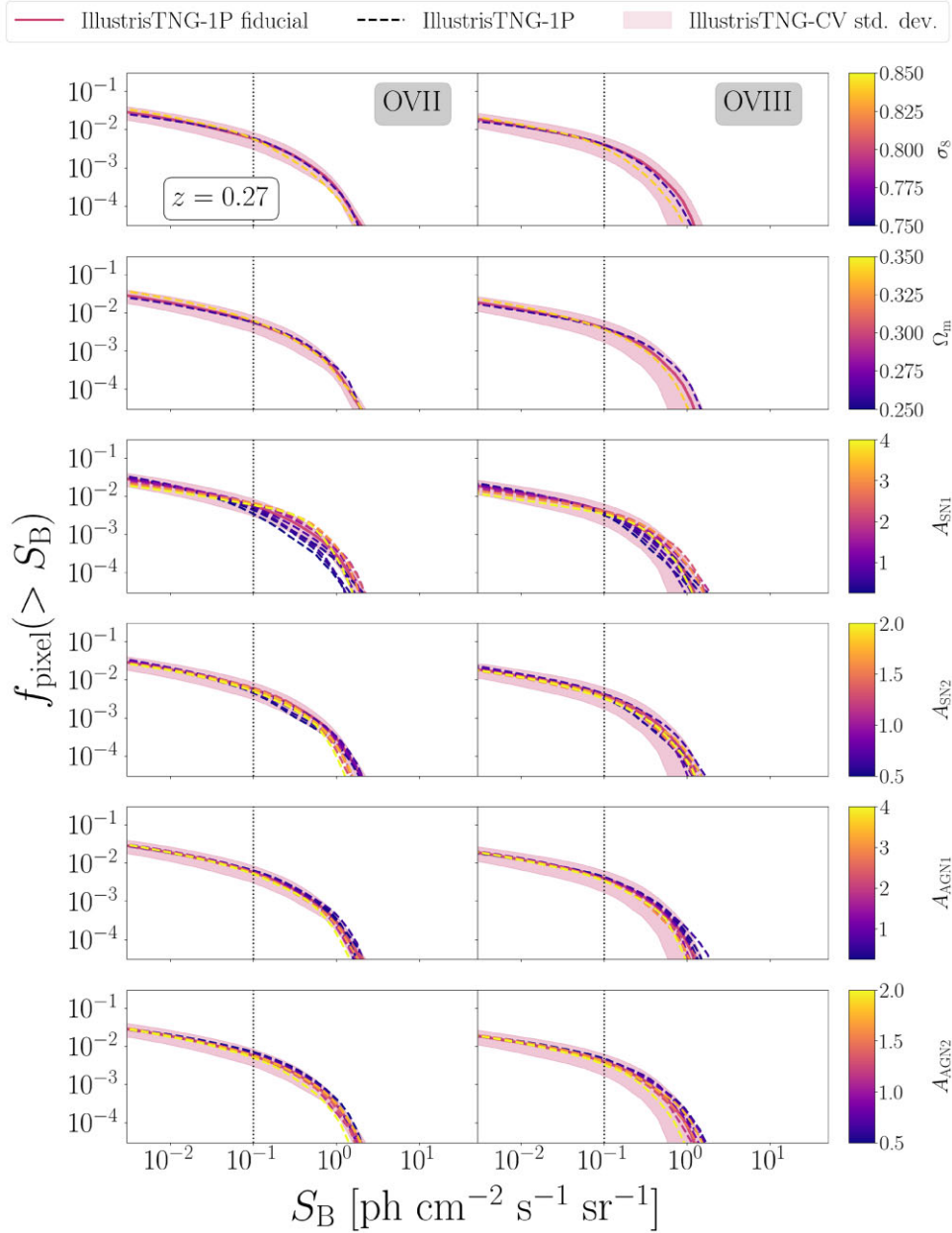
Figure 5. $\log N - \log S_B$ statistics for OVII (left-hand panels) and OVIII (right-hand panels) line counts in the IllustrisTNG-1P subset. In each row the variation of a single parameter with respect to the fiducial model is shown, colour-coded according to the parameter value. The IllustrisTNG-1P prediction is surrounded by a purple shaded area representing the standard deviation as measured from the *rms* scatter among the 27 realizations of the IllustrisTNG-CV subset. The vertical black dotted line identifies the expected 3-σ detection threshold of a 100 ks observation with Athena.

bright regime ≥ 1 ph cm^{-2} s^{-1} sr^{-1}, where the effects of the energy release processes are expected to be larger. However, one can look further into this regime by relaxing the definition of the WHIM gas and consider emission from particles with *total* (rather than only gas) mass overdensity smaller than 1,000. Doing so allows us to probe regions of higher density, in which AGN and stellar feedback processes are strong enough to change the density of the gas but not that of the dark matter. The resulting $\log N - \log S_B$ counts and their trend are qualitatively similar to those of Fig. 6. However, the difference with respect to the fiducial model in the bright counts regime are much larger, boosting up to $6 - 8$ times the cosmic variance level.

4.3 The spatial auto and cross 2-point correlation functions

In the surface brightness maps the intensity of the oxygen line emission peaks in correspondence to the position of the dark matter haloes. This association reflects an underlying spatial correlation that one cannot measure directly because of the finite energy resolution of the X-ray imaging spectrometers. However, nothing prevents us from doing so in the simulations. We show in Fig. 7 the monopole and quadrupole moments of the 2-point autocorrelation function of the OVII line surface brightness fluctuations (left-hand column) and the cross-correlations function of OVII (center) and OVIII (right) line surface brightness fluctuations and the fluctuations in the number density of the haloes. All these quantities are defined at the $N_{\text{grid}} =$
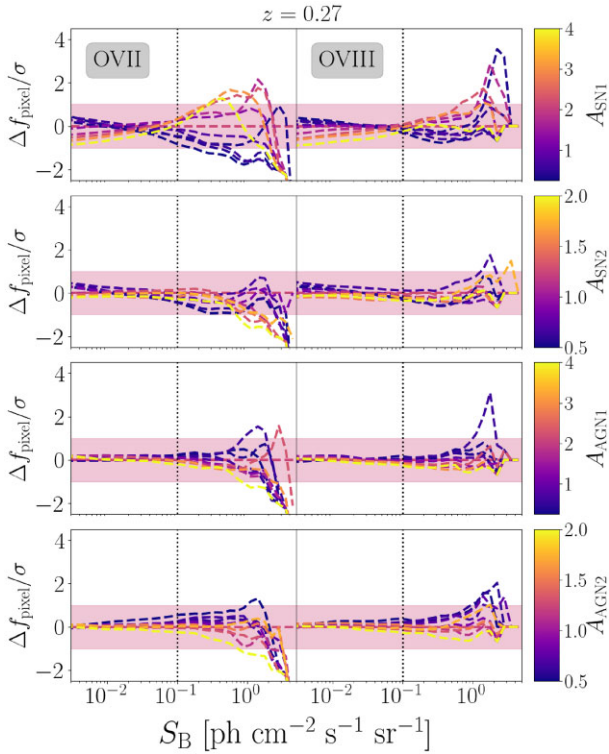
Figure 6. This figure reproduces the lower four panels of Fig. 5, where we show $\log N - \log S_B$ when varying the feedback parameters. Here however we highlight the relative differences of $\log N - \log S_B$ with respect to the fiducial model in units of the statistical uncertainty measured from the CV set.

512^3 gridpoints of the simulation box. Only emission from the WHIM gas has been considered. Results are divided in three rows, each one showing a different redshift snapshot indicated in the labels. For each redshift we show both the monopole (upper panel) and quadrupole (lower panel) moments.

In the plots we use the same colour code as in the previous figures. The IllustrisTNG-CV results are similar to the SIMBA-CV ones at all redshifts, except for the quadrupole moment of the cross-correlation at very small separations. This is remarkable: the correlation properties of the emitters are similar in the two simulations whereas their $\log N - \log S_B$ are different. The monopole moments of the auto- and cross-correlation functions have the familiar power-law shape for separations below ~ 7 Mpc/h), followed by a transition to negative values. This transition is an artefact induced by the so-called integral constraint, i.e. the fact that 2-point function integrated over the sample volume must vanish. The small size of the simulation box places this zero crossing scale at separations much smaller than in the typical clustering analyses over cosmological volumes. As the correlation amplitude at small separation increases with the redshift, the zero crossing scale decreases.

The integral constraints does not apply to the quadrupole moment. That is to say that the zero crossing, in this case, is a genuine feature that marks the transition between small scales characterized by incoherent motions within high density structures and large-scale coherent matter infall towards high density regions. The zero crossing scale decreases with the redshift, which indicates that incoherent motions becomes progressively confined to more compact, virialized structures as a result of the halo merging process, whereas the WHIM gas is coherently accreted onto the nodes and the filaments of the

large-scale structure. Interestingly, in the cross-correlation the zero crossing occurs at smaller separation than in the autocorrelation. This suggests that the relative motion of the collisional gas particles are typically less coherent than that of the gas with respect to the collisionless haloes.

Finally, we note the similarity between the OVII-halo and OVIII-halo cross-correlation functions (and consequently between the OVII-OVII and OVIII-OVIII autocorrelation, not shown). This is a bit surprising, since OVIII emitters are expected to preferentially populate virialized regions where the fraction of OVII ions is lower. Yet this result is robust, since it is obtained from both simulation sets, and statically significant since, as is seen in Fig. 7, the signal to noise is clearly boosted by the cross-correlation, in comparison to the autocorrelation case.

4.4 The angular auto and cross 2-point correlation functions

Integral field spectroscopy will allow us to map the line emission within redshift slices whose thickness is determined by the energy resolution of the instrument. As a result, one will be able to perform a tomographic, rather than 3D analyses, by measuring the angular correlation function of the line surface brightness maps (and the cross correlation with the halo centers).

In Fig. 8 we show the results of the analysis. The 2-point auto and cross angular correlation functions shown here are the projected versions of the spatial ones shown in Fig. 7. We observe the same features that we have already described in the previous section: the presence of a zero crossing induced by the integral constraint, the consistency between the IllustrisTNG-CV and the SIMBA-CV predictions, and the similarity between the OVII and OVIII-halo cross-correlation functions, i.e. the fact that the projected density profile of the WHIM around the halo centers can be traced using either the OVII or OVIII lines. Projection effects magnifies a feature barely visible in the spatial correlation function: the core-shaped profile of the inner region. This is very evident for the cross-correlation but also present in the autocorrelation, especially at low redshifts. A similar feature was seen in the OVII-OVIII and OVIII-OVIII autocorrelation measured in the IllustrisTNG simulation by Nelson et al. (2018b) (see their fig. 7). The likely explanation is that the core-shaped profile indicates that the fraction of OVII and OVIII ions decreases when moving towards the center of dark matter haloes where the temperature and the gas density steadily increase.

Although we are not attempting to provide realistic forecast to future observations, it is important to note that the signal-to-noise of the angular cross-correlation is higher than that of the autocorrelation. This result suggests that an effective strategy to indirectly detect the WHIM and to study its spatial distribution in relation to that of haloes is to cross-correlate the observed surface brightness maps with the angular distribution of galaxies in the same redshift slice taken from existing (or follow-up) spectroscopic, or photometric, galaxy redshift catalogues.

In the last figure of this section we show how the angular correlation functions depend on the parameters of the models. The results are summarized in Fig. 9. We show the angular autocorrelation of the OVII surface brightness (left-hand column) and the halo-OVII cross-correlation (right-hand column) for various choices of σ_8 and Ω_m (upper two rows) and of the parameters that regulate the energy feedback. Colour codes and line styles are the same as in Fig. 5. We do not show the OVIII results since they are very similar to those of the OVII emitters.

Contrary to the $\log N - \log S_B$ case, the angular correlation properties are more sensitive to changes in the cosmological model
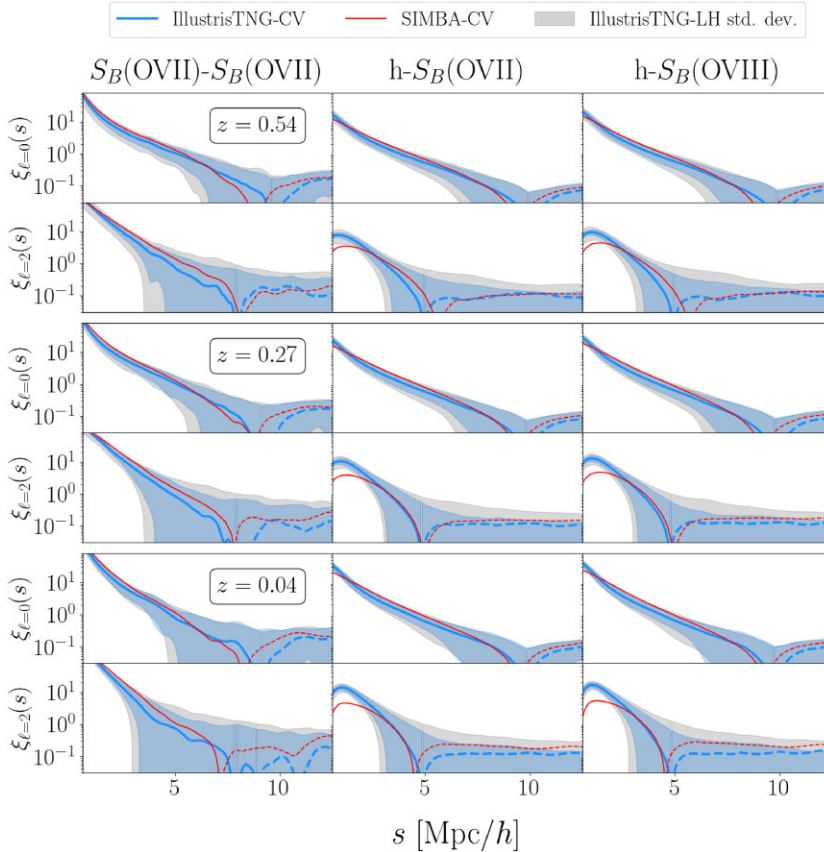
Figure 7. 3D auto- and cross- 2-point correlation function of WHIM line emission and haloes. The figure is divided in three part. The top and the bottom plots of each one show the monopole and quadrupole moments of the OVII line S_B autocorrelation (left-hand panels) and halo-S_B of OVII and OVIII cross-correlations (central and right-hand panels, respectively) at $z = 0.54, 0.27, 0.04$ (top, middle and bottom row, respectively). Cyan (red) curves show the average measurement over the 27 IllustrisTNG-CV (SIMBA-CV) realizations. Solid lines indicate positive correlation. Dashed line is for negative correlation. Cyan and grey shaded areas quantify the *rms* scatter among the 27 and 63 IllustrisTNG-CV and IllustrisTNG-LH realizations, respectively.

than in the energy release mechanisms. Increasing either σ_8 or Ω_m has the effect of reducing the correlation amplitude at small angular scales, in both the auto- and the cross-correlation functions. This seems counter intuitive, since both parameters regulate the clustering of the matter. However, a larger clustering amplitude means that haloes virialize, increase their mass and temperature earlier on and consequently reduce the OVII and OVIII ionization fractions. On the contrary, the clustering properties of the emitters are remarkably insensitive to the details of the energy feedback processes. We only detect a positive correlation amplitude at small angular scales on the energy release from star formation (A_{SN1}) but the dependence is weak and well within the standard deviation strip.

The different sensitivity of $\log N - \log S_B$ and $w(\theta)$ on the cosmological and astrophysical parameters is remarkable. It suggests that the combination of the two observations, together with their redshift dependence, has the potential of removing parameters' degeneracy and effectively constrain the most uncertain aspect of the WHIM models: how and where the energy release from star formation processes and AGN activity affect the evolution of the missing baryons in the Universe.

4.5 Sensitivity to the survey volume

The limited volume of the simulation box in the CAMELS suite potentially affects the properties of the WHIM. First of all, neither the individual simulations nor, possibly, their average over the

set of the 27 IllustrisTNG-CV and SIMBA-CV realizations are representative of the cosmic mean. Second, these simulations neglect the contribution of the large-scale modes, potentially biasing the WHIM properties and their summary statistics.

To assess the volume effect we have repeated the same analysis using the TNG300 simulation (Nelson et al. 2019). The volume of this simulation is ~550 larger than that of the CAMELS and the mass resolution is also higher, which allows us to assess both the volume and mass resolution effects in one go.

4.5.1 $\log N - \log S_B$

In Fig. 10 we compare the average $\log N - \log S_B$ of the oxygen line counts at $z = 0.27$ in the 27 IllustrisTNG-CV realizations (thick solid cyan curve, form Fig. 4) with the same counts in the TNG300 simulations. Continuous curves accounts for line emission for the WHIM only, while dashed curves accounts for contribution from all gas particles. The standard deviation shaded areas and their colours are the same as in Fig. 4. The match between the two sets of curves is remarkable. It shows that the IllustrisTNG-CV realizations are not appreciably affected by volume and mass resolution effects. Some difference can be appreciated in the rare counts of bright lines emitted by all gas particles. In this case the average line counts in the small boxes are systematically below those in the larger TNG300 box, although the size of the effect is smaller than the expected uncertainty (not shown to avoid overcrowding the plots).
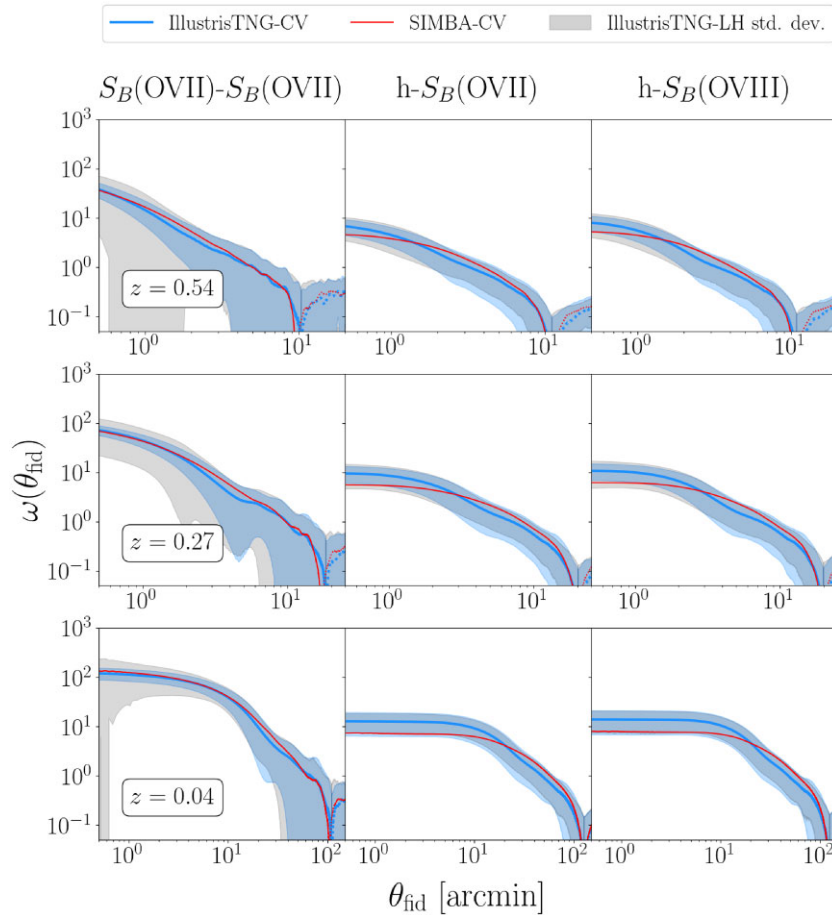
Figure 8. Angular 2-point correlation function of the OVII WHIM line surface brightness (panels on the left) and cross-correlation of the OVII and OVIII WHIM lines and the haloes in the simulations (panels at the center and on the right, respectively). The plots ion the three rows show the measured correlation at the redshifts of three different snapshots: $z = 0.54, 0.27, 0.04$ (top, middle and bottom row, respectively). In each panel the cyan (red) curves represent the average correlation function measured among the 27 IllustrisTNG-CV (SIMBA-CV) simulations. Cyan and grey bands show the *rms* scatter among the 27 IllustrisTNG-CV and 63 IllustrisTNG-LH realizations, respectively.

4.5.2 Angular 2PCF

The results shown in Fig. 11 quantify the sensitivity of the angular auto- and cross-correlation functions to the volume of the $z = 0.27$ box (as we verified the results do not depend ion the redshift). The TNG300, IllustrisTNG-CV and SIMBA-CV angular correlation functions (blue, black and red curves) agree with each other below ~ 10 arcmin within the uncertainty. The former has a larger amplitude than the IllustrisTNG-CV and, especially, the SIMBA-CV ones, reflecting the paucity of large haloes in the small simulations boxes that, instead, are included in the TNG300 snapshots.

On larger angular scales the TNG300 angular correlation steadily decreases but remains positive whereas the other become negative. The zero crossing is a manifestation of the integral constraint that, in the case of the larger TNG300 simulations, is much weaker and pushes the zero crossing up to larger scales.

4.6 The halo-WHIM connection: a closer look

Our results show that a significant fraction of the line emitting gas that could be detected in the near future, is located within or nearby dark matter haloes. We take advantage of the sample of more than 1 million haloes in the TNG300 simulation to investigate the halo-

whim connection in more detail and estimate the fraction of the line emission generated by gas within haloes of a specified mass and that for this reason, could be regarded as CGM.

To do so we have generated a new set of OVII and OVIII surface brightness maps using only WHIM particles within haloes of a given mass. To decide if a gas particle belongs to a halo we have adopted two criteria. The first one considers all particles within the halo virial radius, R_{200m}, within which the mean density is 200 times larger than the cosmic mean. The second one considers instead the 'splashback radius' R_{sp}, defined as the distance at which the accreted matter particles' orbits reach the first apocenter after turnaround. In correspondence of this radius the density profile of the halo becomes steeper than isothermal (dlog ρ/dlog $r < -4$), providing an effective boundary to the structure. The values of R_{200m} and R_{sp} are not independent and several fitting formulae have been proposed to specify their relation and their dependence on the mass accretion rate. Common to these expressions is the inequality $R_{sp} \lesssim 1.9\,R_{200m}$ which holds true even in the most extreme accretion cases. Here, to be conservative and for the sake of simplicity we define and effective splashback radius $R_{sp} \equiv 2 \times R_{200m}$.

The volume filling gas particles in these regions mostly belong to the CGM. The complete identification with this important reservoir of the missing baryons is hampered by the lack of a unique definition of
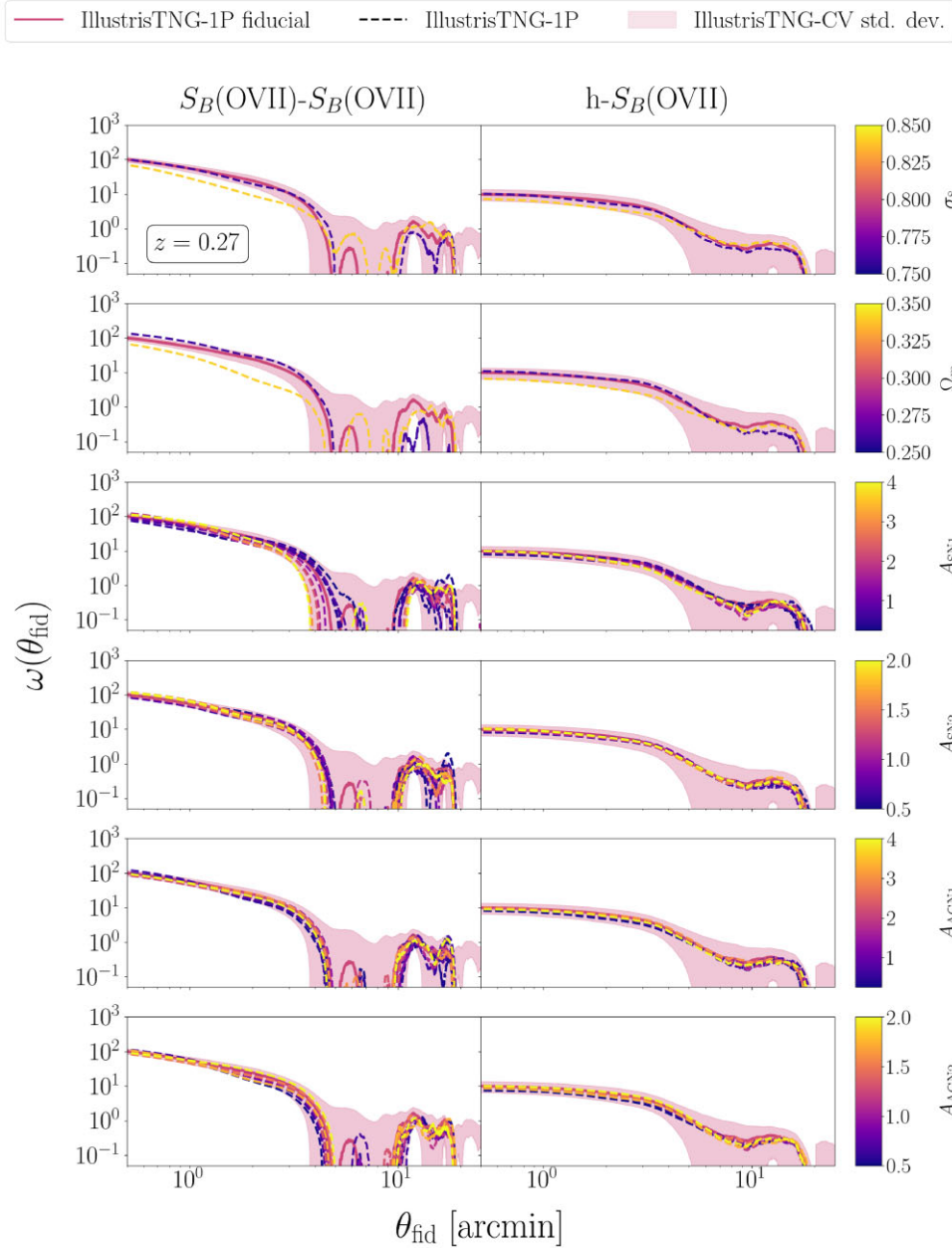
Figure 9. Angular auto- 2-point correlation function of the OVII WHIM line surface brightness (left-hand panels) and OVII-halo cross-correlation (right-hand panels) measured in the IllustrisTNG-1P simulations. In each row the effect of varying one parameter of the model, indicated on the right Y-axis, is shown. The colour code and the meaning of the coloured band are the same as as in Fig. 5.

the CGM in the literature (see e.g.(Truong et al. 2020; Comparat et al. 2022)). One of our definitions, the one that uses R_{200m}, is very similar to the one adopted by Wijers & Schaye (2022) to investigate the CGM properties in the **EAGLE** simulations. The second definition, that relies on the spashblack radius, is meant to account for the possibility that the CGM distribution extends to a larger region. Having adopted both helps us to quantify the detectable fraction of CGM gas and its uncertainty.

In Fig. 12 we show the $\log N - \log S_B$ of the lines generated within haloes if different masses. The thick black curves represent the $\log N - \log S_B$ of all OVII (left-hand panels) and OVIII (right) WHIM line counts TNG300 snapshot at $z = 0.27$. The thin black lines show the $\log N - \log S_B$ counts from gas particles within R_{200m} (left-hand

panels) and within R_{sp} (right). Clearly, only a minor, though sizable, fraction of line counts are fully (or mainly) contributed by gas within a halo. The majority of the counts are contributed by several structures along the line if sight, not all of them necessarily associated with haloes. This fraction is larger than 50 per cent for gas within R_{sp}, but never dominates the total line count budget.

The curves with different colours show the contribution from gas within haloes in a specific mass range, indicated in the label. Interestingly, the magnitude of the contribution increases with the mass of the halo. It is largest for haloes in the mass range $10^{12} - 10^{14} \, M_\odot/h$ and then suddenly drops. This is not surprising since the gravitationally bound mass in OVII and OVIII is remarkably constant for halo masses larger than $10^{12} \, M_\odot/h$ and then decreases
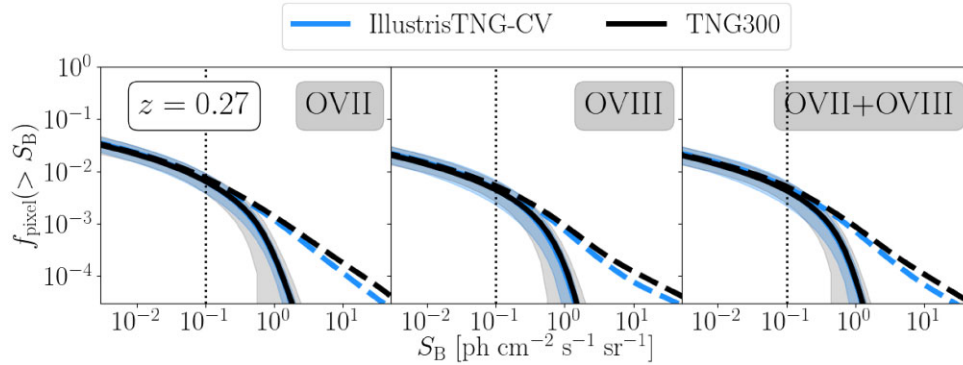
Figure 10. Comparison between the fraction of WHIM emitters in OVII (left), OVIII (middle) and both (right) for a snapshot at $z = 0.27$ of the TNG300 (black solid lines) and the mean of the 27 realizations of the IllustrisTNG-CV set (blue solid lines). Dashed lines refer to all the gas particles. Blue and grey shaded areas surrounding the lines represent the scatter of the IllustrisTNG-CV and IllustrisTNG-LH sets, respectively. The vertical dotted black line marks the Athena sensitivity.
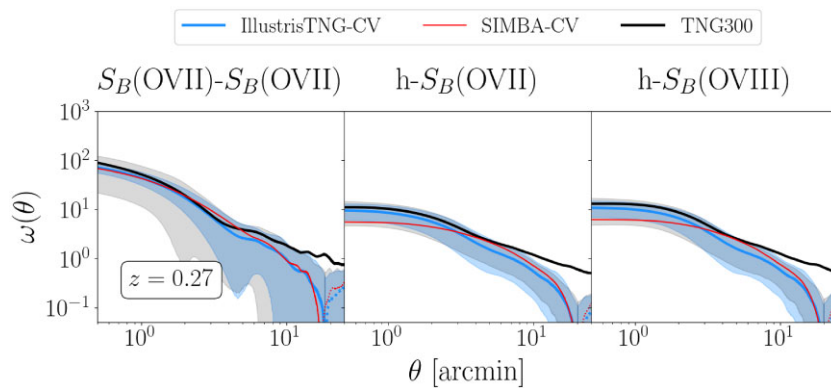

Figure 11. Comparison of the angular 2PCFs for S_B of OVII (left-hand panels) and halo-S_B of OVII and OVIII (central and right-hand panels, respectively) for the TNG300, IllustrisTNG-CV and SIMBA-CV simulations. We show here the snapshot at $z = 0.27$. Blue lines and shaded area represent the mean and scatter of the 27 realizations of the IllustrisTNG-CV subset; red lines do likewise for the SIMBA-CV subset. The grey shaded area is the scatter of the IllustrisTNG-LH simulations we consider. The solid black line is the measurement from the TNG300 simulation.

for lower masses (Nelson et al. 2018b). The small contribution from very massive haloes just reflects the paucity of these rare structures.

To further inspect the gas properties in the vicinity of dark matter haloes we compare the line counts within $R_{\rm sp}$ with the counts within $R_{\rm 200m}$, effectively sampling the density profile of the emitting gas in the outer region of the haloes. The result is shown in Fig. 13 in which we plot the ratio of the counts as a function of the halo mass. The ratio is not constant. It decreases from ~8 to a value of about 4, featuring a sudden drop at $10^{11} M_\odot/h$. The value ~4 measured for large haloes is what one expects for an isolated halo following an isothermal density profile in the interval $[R_{\rm 200m}, R_{\rm sp}]$. This means that the line emitting gas particles do belong to the halo. On the contrary, the larger ratio ~8 associated with less massive haloes indicates that a significant fraction of the line emitting gas mass is associated with the surrounding large-scale structure rather than to the halo itself.

Fig. 14 clarifies this point further. It shows the angular OVII-halo angular cross-correlation function for halo of different masses, i.e. the angular surface brightness profile of the WHIM OVIII emission around haloes in the same mass ranges as in Fig. 13. The different brightness profiles have similar shapes: a central core-like structure followed by a power-law decrease. Less massive haloes have shallower profile, whereas the central region of the the more massive ones could not be probed because of the large halo-OVII

emitter mean separation. The point is that the $[R_{\rm 200m}, R_{\rm sp}]$ interval corresponds, for small haloes, to sampling the core-like region where the OVII surface brightness profile is shallower. On the contrary, for larger haloes, the same range of physical separations probes the outer region of the surface brightness profile, where the slope is steeper. That is to say, a significant fraction of the line emitting gas is associated with the the large-scale structures (outer halo regions, filaments) rather than to the halo itself. We conclude that the brightest spots in the surface brightness maps are mostly associated with the gas within the large haloes. On the contrary, the emission associated with smaller structures is significantly contributed by gas that belong to large-scale structures.

5 LOG N − LOG S_B FORECAST ON A LIGHT-CONE

So far we have simulated surface brightness maps at well-defined redshifts, obtained from a few selected snapshots of the CAMELS simulations. Real maps will, instead, account for line emission from all redshift along the light-cone. Therefore, to obtain more realistic predictions on the possibility of studying the WHIM in the X-ray band and to compare our results with those in the literature, we decided to simulate the surface brightness maps of the OVII and the OVIII lines from all the gas particles along the line of sight to $z =$
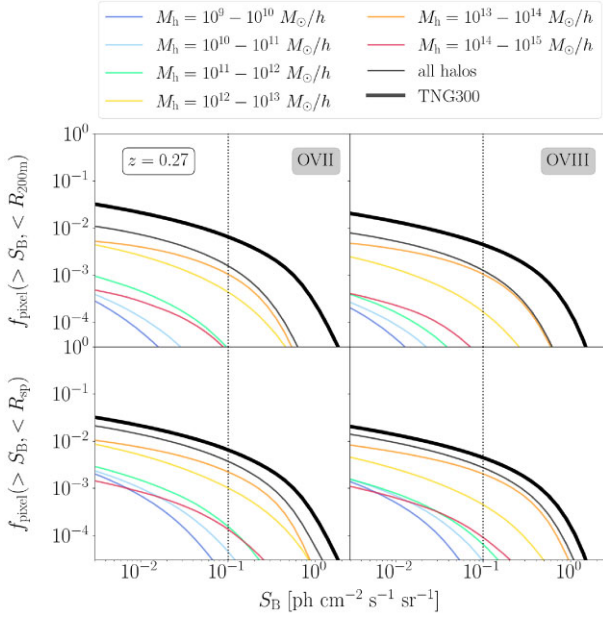
Figure 12. *Top:* Surface brightness $\log N - \log S_B$ in the TNG300 simulation. The thick black solid line shows the $\log N - \log S_B$ of WHIM particles in the TNG300 slice. The vertical grey shaded area is the S_B region not observable by Athena. Thinner lines display the X-ray emission coming from WHIM particles found inside haloes (within R_{200m}) of different mass decades. *Bottom:* Same as top, but thinner lines display the emission from WHIM particles inside R_{sp}.
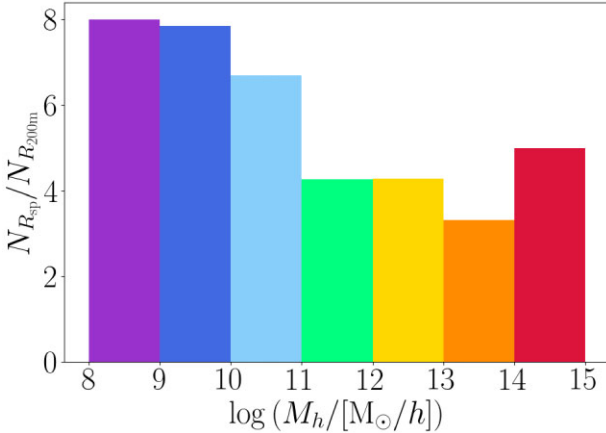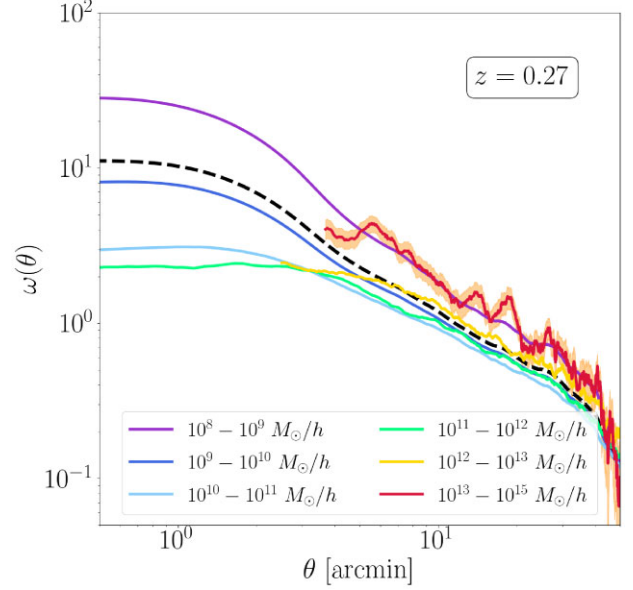

Figure 14. Angular cross-correlation between OVII emitters and the centers of dark matter haloes of different masses in the TNG300 snapshot at $z = 0.27$. Different colours identify different mass ranges, indicated in the label. The colour code is the same as in Fig. 12. Haloes with mass in the mass range $[10^{13}, 10^{15}]\ M_\odot/h$ have been grouped together because of their limited number. The orange strip around the ref curve shows the scatter estimated from 196 jackknife resampling the same halo-emitter data sets. The thick dashed line is represents the cross-correlation of all OVII emitters with all the haloes in the sample.

Figure 13. Histogram representing the ratio between number of WHIM particles within R_{sp} ($N_{R_{sp}}$) and that of the particles within R_{200m} ($N_{R_{200m}}$) estimated for haloes in different mass ranges, indicated in the X-axis. The colour code is the same as in Fig. 12.

0.54. To do so we have rearranged the various simulated outputs into a light-cone using the approximated procedure described below. We built two types of light-cones: those obtained from 9 snapshots of the IllustrisTNG-CV simulations set and the one obtained from the 32 snapshots of the TNG300 simulation. The procedure adopted is the same in both cases, only the thickness of the snapshots slices piled up to build the cone is different. Also, since our procedure relies on the line counts performed on the individual snapshots, for which we have assumed the distant observer hypothesis, we cannot use the very nearby $z = 0$ snapshot and build the light-cone using only the simulation outputs in the range $0.05 \leq z \leq 0.54$. The procedure

to simulate the brightness maps and estimate the line counts is as follows:

(i) We define the footprint of the light-cone. This is a squared area with an opening angle $\arctan\left(\frac{L/2}{\chi(z=0.05)}\right)$, where $\chi(z = 0.05)$ is the comoving distant to the redshift to the nearest snapshot in the cone.

(ii) Given the available snapshots, we define the redshift interval $[z_{i-1}, z_i]$, where z_i is the redshift of a snapshot, except for $z_i = 0.05$ for which the corresponding simulation snapshot is the one at $d = 0$.

(iii) Having defined the area and the thickness of all non-overlapping slices we estimate their individual volume V_i.

(iv) We rescale the oxygen line counts already performed on each snapshot $N(> S_B, z_i)$ to the volume of each redshift slice $N_i(> S_B, z_i) \rightarrow N(> S_B, z_i)\frac{V_i}{L^2 \Delta L}$, where ΔL is the thickness of the simulation slice at each redshift (see Table 1).

(v) We repeat the procedure for all the slices, sum over, divide by the number of pixels in the footprint and obtain the number of OVII and OVIII lines brighter than S_B per line of sight shown in Fig. 15.

The thick line in the plots represents the $\log N - \log S_B$ of the OVII (left), OVIII (center) and joint OVII + OVIII (right) line counts from the light-cone extracted from the TNG300 simulation. The size of the simulation box is about 6 times smaller than the comoving distance to $z = 0.05$, which inevitably implies some replication of the same structures in the light-cone. Since we are interested in the line counts only, we made no attempt to rearrange the orientation of the slices across the cone. On the other hand, replicating the same structures artificially removes cosmic variance, to appreciate which we use the 27 light-cones obtained from the IllustrisTNG-CV simulations. The resulting average counts predictions are represented
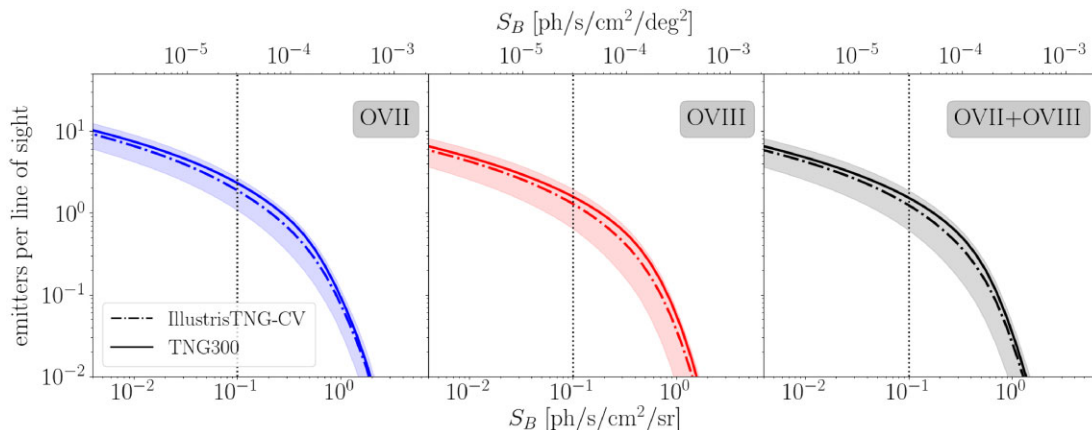
Figure 15. Number of WHIM emitters in OVII (left), OVIII (center) and OVII + OVIII (right) per line of sight as a function of surface brightness in a light-cone to $z = 0.54$. Predictions from the TNG300 (continuous curves) and IllustrisTNG-CV (dashed) simulations are shown surrounded by a shaded region representing the *rms* scatter among the 27 IllustrisTNG-CV realizations. The vertical black dotted line identifies the expected 3-σ detection threshold of a 100 ks observation with Athena.

by the dashed curves in the panels and the surrounding shaded areas the magnitude of the cosmic variance. It is reassuring that both $\log N - \log S_B$ curves, from the IllustrisTNG-CV and the TNG300 light-cones are consistent with each other. Both exhibit a characteristics double power-law shape with a knee at $S_B \sim 0.3 \, \mathrm{ph \, cm^{-2} \, s^{-1} \, sr^{-1}}$ beyond which the line counts become more rare. With the X-IFU 3-σ sensitivity threshold set at $S_B \sim 0.1 \, \mathrm{ph \, cm^{-2} \, s^{-1} \, sr^{-1}}$ for a 100 ks observation with Athena (vertical grey band) the number of expected detections per pixel is in the range [1,3] for OVII and [1,2] for OVIII (and OVII+OVIII). Multiplying by the number of pixels in the X-IFU field of view (with a diameter of 5 arcmin) we then expect [3600,10800] OVII detections and [3600,7200] OVII (and OVII + OVIII) detections in total.

These counts, however, should not be regarded as independent since in most cases line emission in nearby pixels is produced by a single physical structure. Previous works have shown that WHIM emitters have a typical angular size of a few arcminutes (Ursino & Galeazzi 2006; Galeazzi, Gupta & Ursino 2009; Takei et al. 2011; Ursino et al. 2011), also confirmed by our angular autocorrelation analysis. For this reasons the first proposals to detect the WHIM in emission with X-ray integral field spectroscopy (like e.g. *EDGE*, Piro et al. (2009), or *Xenia*, Burrows et al. (2010)) were designed to have a matching angular resolution and theoretical forecast where provided accordingly. As a result, to compare our $\log N - \log S_B$ with those of Takei et al. (2011) we had to rescale our predictions to the angular resolution of 1.3 arcmin of their simulated maps. The results are shown in Fig. 16 where, along with our original counts in 5 arcsec pixels (continuous dark curves) we show the counts in the larger 1.3 arcmin pixels (continuous light curves), both superimposed to the $\log N - \log S_B$ reported from model B2 of Takei et al. (2011) also estimated from a map with 1.3 arcmin resolution. All curves account for the number of OVII and OVIII emission lines generated by WHIM gas in a light-cone out to $z = 0.54$.

Decreasing the angular resolution increases the faint line counts and decreases the bright ones. This is not surprising. The integrated emission over a 1.3 arcmin regions will generally be composed by a number of brighter and fainter pixels that contribute to correspondingly bright and faint counts in the 5 arcsec resolution $\log N - \log S_B$ curves. The comparison with the result of Takei et al. (2011) shows that the two predictions are quite similar for the faint counts whereas in the bright end we predict systematically
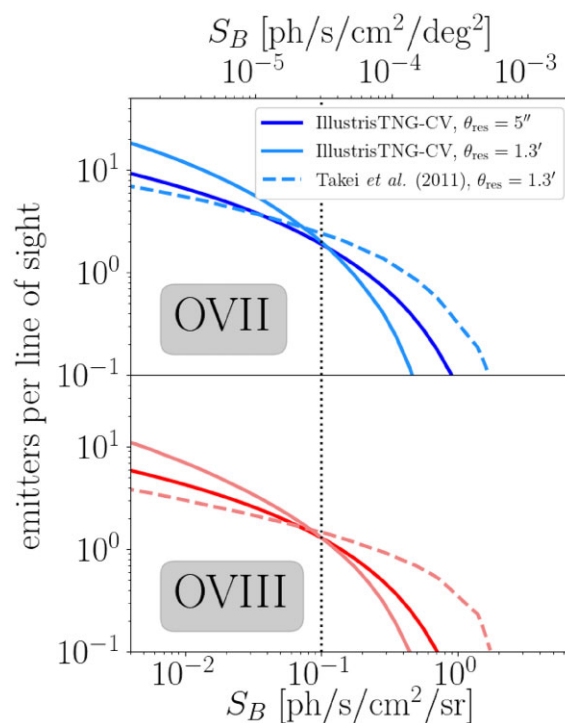

Figure 16. $\log N - \log S_B$ curves for OVII (top panel) and OVIII (bottom) representing the average line counts in pixels of angular size 5 arcsec (dark curves) and 1.3 arcmin (light curves) in the IllustrisTNG-CV realizations. The dashed curve is plotted for reference and represents the analogous $\log N - \log S_B$ counts of Takei et al. (2011) as shown in fig. 2 of their paper.

less counts, regardless of whether we use of IllustrisTNG-CV or SIMBA-CV. This mismatch is not surprising. Roncarelli et al. (2012) also noticed that the bright counts of Takei et al. (2011) B2 models were systematically larger than theirs. The likely explanation is related to the details of the WHIM model. Part of the reason is related to the simulation technique: the model of Takei et al. (2011) relies on the hydrodynamic simulations by Borgani et al. (2004) which uses the GADGET-2 (Springel 2005) code, as opposed to the IllustrisTNG simulation that have been performed with the AREPO code. However, this fact alone does not explain the mismatch, since

as we already mentioned using the counts from the SIMBA-CV maps instead of the IllustrisTNG-CV ones would not erase the difference. The main effect is likely related to the treatment of the gas metallicity. Takei et al. (2011) did not assign gas metallicity in a self-consistent fashion. They did so in the post-processing phase using the phenomenological density–metallicity relations derived from the Cen & Ostriker (1999b) hydrodynamic simulation. (Roncarelli et al. 2012) Roncarelli et al. (2012) showed that the large scatter of that relation, assumed to be Gaussian, artificially enhanced the gas metallicity in low density environment, making the WHIM emission brighter.

One remarkable feature, though, is the fortuitous crossing of the various $\log N - \log S_B$ curves in correspondence to a surface brightness value similar to the Athena X-IFU detection threshold, which implies that the number of expected detections per line of sight is similar to that predicted by Takei et al. (2011) and insensitive to the angular resolution of the map.

6 DISCUSSION AND CONCLUSIONS

There is now a general consensus that the bulk of missing baryons are to be found in the form of a highly ionized warm hot gas in the intergalactic medium and in the CGM that could be effectively probed by means of X-ray spectroscopy. A few detections along two sightlines, however, are largely insufficient to address all the open issues regarding the spatial distribution of baryons in the late Universe, their ionization state, metal enrichment and thermal history. Only next generation instruments will be able to tackle the problem by combining absorption studies capable to probe missing baryons in moderate density environments along selected sightlines and observations of line emission of the gas in high density regions. The possibility of performing X-ray integral field spectroscopy with proposed space missions like XRISM (XRISM Science Team 2020) and, especially, Athena (Nandra et al. 2013) and LEM will give us such opportunity.

Several works have used hydrodynamic simulations to investigate the issue using absorption spectra. In this work we took advantage of the availability of a very large number of hydrodynamic simulations produced by the CAMELS project (Villaescusa-Navarro et al. 2020, 2022), to systematically investigate the properties of the WHIM in emission over a wide range of scenarios characterized by different choices of cosmological parameters as well as stellar and AGN energy feedback models. The possibility of comparing results obtained using identical conditions but different simulation techniques provides us with the unique opportunity to assess the adequacy of the numerical models and their robustness to the choice of the free parameters.

One important aspect of the CAMELS simulations is the size of the computational box, 25 comoving Mpc/*h*, which is much smaller than the size of a typical cosmological simulation but more than adequate to investigate the possibility of studying the WHIM in emission in future observations considering the limited field of view of next generation instruments (∼5 arcmin² in the original Athena X-IFU design).

The main results of our analysis are as follows:

(i) The OVII and OVIII line emission above detection threshold peaks in correspondence to the position of the dark matter haloes, in agreement with Takei et al. (2011) results. There is little evolution of both lines' surface brightness out to $z \simeq 0.5$ which confirms the results of Martizzi et al. (2019), and little dependence on the cosmological parameters σ_8 and Ω_m.

(ii) The $\log N - \log S_B$ of the line counts are sensitive to the details of the hydrodynamical simulation. Line counts in the IllustrisTNG-CV realizations are significantly larger than in the SIMBA-CV ones, a difference that quantifies the current uncertainties in modelling the properties of the WHIM and the CGM in the simulations. Line counts are robust to varying the values of σ_8 and Ω_m and ti the size of the simulation bix. However, they are sensitive to the energy feedback processes. The latter dependence is not intuitive: a larger energy injection through star formation and supernovae explosions increases the number of bright line count but the opposite effect is seen when the energy is released by AGN activity.

(iii) The spatial correlation properties, quantified through the spatial 2-point correlation function, of the line emitting gas are quite similar in the IllustrisTNG-CV and the SIMBA-CV simulations. And so is their cross-correlation with the haloes' positions. The analysis of the quadrupole moment reveals that near the center of the haloes the gas dynamics is characterized by incoherent motions whereas the outer regions are characterized by a coherent infall of the gas, presumably associated with mass accretion from the large-scale filaments.

(iv) The analysis of the angular 2-point correlation function, the only 2-point statistics actually measurable with current and next generation X-ray spectrographs, shows that the autocorrelation signal of the OVII and OVIII is potentially detectable by next generation instruments. Its signal-to-noise is even larger when the surface brightness maps are correlated with the position of the haloes. This suggests that a possible strategy to indirectly detect the WHIM, alternative to the stacking technique (Tanimura et al. 2020) is to cross-correlate the observed X-ray emission maps with the angular position of galaxies within self-consistent energy/redshift bins for a tomographic clustering analysis similar to the one commonly performed with galaxies whose redshift has been estimated through multiband photometry rather than spectroscopy.
The amplitude of angular auto- and cross- 2-point correlations increases with σ_8 and Ω_m but is insensitive to the amount of energy released in the medium by the star formation process and AGN activity. A possible interpretation for this insensitivity is that the spatial correlation properties of the line emitting gas are largely determined by the gas accretion processes and subsequent formation of the shock fronts that are quite insensitive to the details of the energy feedback processes.

(v) We found that a significant, though not dominant, fraction of the WHIM emission comes from within the virial radius or from twice that distance, corresponding to the splashback radius. Most of this emission is associated with haloes in the mass range $10^{12}-10^{14}\,M_\odot/h$ and follows the mass–density profile of the halo itself. The remaining, minor contribution to the line emission is associated with smaller haloes but seems more extended than their physical size and likely associated with the surrounding large-scale structures.

(vi) We have compared our $\log N - \log S_B$ with those of the Takei et al. (2011) model at $z = 0.54$ for an angular resolution of 1.3 arcmin. The cumulative number counts of the two models are consistent with each other at the fiducial detection threshold of 0.1 photons cm^{-2} s^{-1} sr^{-1}. However, the number of bright counts of Takei et al. (2011) is significantly larger than ours. A similar mismatch was already noticed by Roncarelli et al. (2012) and attributed to the gas metallicity which, in their case, was not estimated self-consistently in the hydro simulations but assigned in the post-processing phase using phenomenological relations.
Next-generation imaging spectrometers, like those proposed for the Athena and the LEM satellite missions, will have an angular resolution higher than the typical size of the line-emitting structures.

This will not increase the WHIM detection probability but will allow one to spot and remove bright, point-like sources like the AGNs and possibly to separate will regions in which the emission is dominated by the diffuse WHIM component from those dominated by the compact CGM using, of course, model-dependent criteria.

In this work we did not attempt to provide realistic forecasts on the ability to detect and study the WHIM in emission with some specific instrument, although we often referred to the case of a 'typical' 100 ks observation with Athena X-IFU. We feel, however, that it will be important to do so in the future, once next generation X-ray instruments will be approved and their technical design will be frozen. It will be important to include a realistic treatment of the foreground emission, especially from the Galaxy, and rederive a more realistic detection threshold for all potentially observable X-ray lines, not just OVII and OVIII. Nevertheless, we believe that the main results of this work that we have summarized above are robust and that our main conclusions will not be significantly modified using more realistic data sets. What we plan to do next is to improve the statistical analysis of the surface brightness maps to increase the statistical significance of the WHIM detection and improve our ability to study its physics. One possibility would be to perform a joint statistical analysis that includes both line counts and angular correlation and their redshift dependence. Additionally, one could combine the line emission analysis with that of other WHIM probes like the Sunayev Zel'dovich effect (Moser et al. 2022). Better still, one could fully exploit the power of the CAMELS simulation suite and apply machine learning techniques to the surface brightness (and possibly Sunayev Zel'dovich) maps to perform field-level likelihood-free inference.

DATA AVAILABILITY

The data generated in this article (surface brightness maps, correlation functions and $\log N - \log S_B$) will be shared on reasonable request to the corresponding author. Brightness maps are originally generated at high angular and energy resolution and can be re binned to match the characteristics of any X-ray imaging spectrometer that may be adopted in future X-ray missions. The CAMELS simulations data are available at https://camels.readthedocs.io.

REFERENCES

Asplund M., Grevesse N., Sauval A. J., Scott P., 2009, ARA&A, 47, 481
Bertone S., Schaye J., Dalla Vecchia C., Booth C. M., Theuns T., Wiersma R. P. C., 2010, MNRAS, 407, 544
Bonamente M., Mirakhor M., Lieu R., Walker S., 2022, MNRAS, 514, 416
Borgani S. et al., 2004, MNRAS, 348, 1078
Branchini E. et al., 2009, ApJ, 697, 328
Burrows D. N., Hartmann D., Kouveliotou C., Piro L., den Herder J. W., Ohashi T., 2010, in Arnaud M., Murray S. S., Takahashi T., eds, Society of Photo-Optical Instrumentation Engineers (SPIE) Conference Series, vol. 7732. Space Telescopes and Instrumentation 2010: Ultraviolet to Gamma Ray. p. 77321T
Cen R., 2012, ApJ, 753, 17
Cen R., Fang T., 2006, ApJ, 650, 573
Cen R., Ostriker J. P., 1999a, ApJ, 514, 1
Cen R., Ostriker J. P., 1999b, ApJ, 519, L109
Chadayammuri U., Bogdán Á., Oppenheimer B. D., Kraft R. P., Forman W. R., Jones C., 2022, ApJ, 936, L15
Comparat J. et al., 2022, A&A, 666, A156
Cyburt R. H., Fields B. D., Olive K. A., Yeh T.-H., 2016, Rev. Mod. Phys., 88, 015004
DES Collaboration et al., 2021, preprint (arXiv:2105.13549)
Davé R., Anglés-Alcázar D., Narayanan D., Li Q., Rafieferantsoa M. H., Appleby S., 2019, MNRAS, 486, 2827
Davis M., Efstathiou G., Frenk C. S., White S. D. M., 1985, ApJ, 292, 371
Foster A. R., Ji L., Smith R. K., Brickhouse N. S., 2012, ApJ, 756, 128
Fukugita M., Hogan C. J., Peebles P. J. E., 1998, ApJ, 503, 518
Galeazzi M., Gupta A., Ursino E., 2009, ApJ, 695, 1127
Hamilton A. J. S., 1998, in Hamilton D., ed., Astrophysics and Space Science Library, vol. 231, The Evolving Universe. p. 185, preprint (arXivastro-ph/9708102)
Hopkins P. F., 2015, MNRAS, 450, 53
Huchra J. P., Geller M. J., 1982, ApJ, 257, 423
Kaastra J. et al., 2013, preprint (arXiv:1306.2324)
Kaiser N., 1987, MNRAS, 227, 1
Kovács O. E., Bogdán Á., Smith R. K., Kraft R. P., Forman W. R., 2019, ApJ, 872, 83
Kraft R. et al., 2022, preprint (arXiv:2211.09827)
Macquart J. P. et al., 2020, Nature, 581, 391
Marinacci F. et al., 2018, MNRAS, 480, 5113
Martizzi D. et al., 2019, MNRAS, 486, 3766
Moser E. et al., 2022, preprint (arXiv:2201.02708)
Naiman J. P. et al., 2018, MNRAS, 477, 1206
Nandra K. et al., 2013, preprint (arXiv:1306.2307)
Nelson D. et al., 2018a, MNRAS, 475, 624
Nelson D. et al., 2018b, MNRAS, 477, 450
Nelson D. et al., 2019, Computational Astrophysics and Cosmology, 6, 2
Nicastro F. et al., 2005, The Astrophysical Journal, 629, 700
Nicastro F., Krongold Y., Mathur S., Elvis M., 2017, Astronomische Nachrichten, 338, 281
Nicastro F. et al., 2018, Nature, 558, 406
Oppenheimer B. D. et al., 2016, MNRAS, 460, 2157
Oppenheimer B. D., Segers M., Schaye J., Richings A. J., Crain R. A., 2018, MNRAS, 474, 4740
Pillepich A. et al., 2018, MNRAS, 475, 648
Piro L. et al., 2009, Experimental Astronomy, 23, 67
Planck Collaboration et al., 2016, A&A, 594, A13
Planck Collaboration et al., 2020, A&A, 641, A6
Rahmati A., Schaye J., Crain R. A., Oppenheimer B. D., Schaller M., Theuns T., 2016, MNRAS, 459, 310
Roncarelli M., Cappelluti N., Borgani S., Branchini E., Moscardini L., 2012, MNRAS, 424, 1012
Shull J. M., Smith B. D., Danforth C. W., 2012, ApJ, 759, 23
Smith R. K., Brickhouse N. S., Liedahl D. A., Raymond J. C., 2001, ApJ, 556, L91
Springel V., 2005, MNRAS, 364, 1105
Springel V., 2010, MNRAS, 401, 791
Springel V., White S. D. M., Tormen G., Kauffmann G., 2001, MNRAS, 328, 726
Springel V. et al., 2018, MNRAS, 475, 676
Stark D. V. et al., 2021, MNRAS, 503, 1345
Takei Y. et al., 2011, ApJ, 734, 91

Tanimura H., Aghanim N., Kolodzig A., Douspis M., Malavasi N., 2020, A&A, 643, L2

Taruya A., Nishimichi T., Saito S., Hiramatsu T., 2009, Phys. Rev. D, 80, 123503

Tepper-García T., Richter P., Schaye J., Booth C. M., Dalla Vecchia C., Theuns T., Wiersma R. P. C., 2011, MNRAS, 413, 190

Treu T. et al., 2022, ApJ, 935, 110

Truong N. et al., 2020, MNRAS, 494, 549

Truong N., Pillepich A., Nelson D., Werner N., Hernquist L., 2021, MNRAS, 508, 1563

Ursino E., Galeazzi M., 2006, ApJ, 652, 1085

Ursino E., Branchini E., Galeazzi M., Marulli F., Moscardini L., Piro L., Roncarelli M., Takei Y., 2011, MNRAS, 414, 2970

Viel M., Branchini E., Cen R., Matarrese S., Mazzotta P., Ostriker J. P., 2003, MNRAS, 341, 792

Viel M., Branchini E., Cen R., Ostriker J. P., Matarrese S., Mazzotta P., Tully B., 2005, MNRAS, 360, 1110

Villaescusa-Navarro F. et al., 2020, preprint (arXiv:2010.00619)

Villaescusa-Navarro F. et al., 2022, preprint (arXiv:2201.01300)

Weinberger R. et al., 2017, MNRAS, 465, 3291

Weinberger R., Springel V., Pakmor R., 2019, preprint (arXiv:1909.04667)

Werner N., Durret F., Ohashi T., Schindler S., Wiersma R. P. C., 2008, Space Sci. Rev., 134, 337

Wijers N. A., Schaye J., 2022, MNRAS, 514, 5214

Wijers N. A., Schaye J., Oppenheimer B. D., Crain R. A., Nicastro F., 2019, MNRAS, 488, 2947

Wijers N. A., Schaye J., Oppenheimer B. D., 2020, MNRAS, 498, 574

XRISM Science Team, 2020, preprint (arXiv:2003.04962)

Zappacosta L., Maiolino R., Mannucci F., Gilli R., Schuecker P., 2005, MNRAS, 357, 929

ZuHone J. A., Hallman E. J., 2016, pyXSIM: Synthetic X-ray observations generator , preprint(ascl1608.002)

This paper has been typeset from a TEX/LATEX file prepared by the author.